Arab American University

Faculty of Graduate Studies

Preparation and Characterization of AgO-As_2O_3 Thin films

By

Mayamen Ibraheem Saeed Abu-Altayeb

Supervisor

Prof. Dr. Atef Fayez Qasrawi

This Thesis was submitted in partial fulfillment of the requirements for

the Master's degree in Physics

August/2021

Preparation and characterization of AgO-As_2O_3 thin films

By

Mayamen Ibraheem Saeed Abu-Altayeb

This thesis was defended successfully on 31st August2021 and approved by:

Committee members	Signature
1. Supervisor: Prof. Dr. Atef Fayez Qasrawi	.....
2. Internal examiner: Prof.Dr. Hazem Khanfar	.....
3. External examiner: Prof.Dr. Mohammad Elsaid	.....

Declaration

The work in this thesis, unless otherwise referenced, is the researcher's own work and has not been submitted elsewhere for any other degree or qualification.

العمل في هذه الرسالة، ما لم تتم الاشارة الى خلاف ذلك، هو عمل الباحث الخاص ولم يتم تقديمه في أي مكان آخر للحصول على درجة أو مؤهل آخر.

Student's Name: Mayamen Ibraheem Saeed Abu-Altayeb

Signature: mayamen

Date: 1.12.2021

Acknowledgment

Praise to God, who gave me the strength, patience and determination to embark on the journey towards obtaining a master's degree.I am deeply thankful to my supervisor, the honorable Professor. Dr. Atef Qasrawi for his support and encouragement, who gave me much of his time and effort in reading, checking and gave me advice and guidance to do my best. Thanks a bunch for all the members of physics department in my prestigious university- Arab American University- and to the Ministry of Higher Education- the institution of my work. Words cannot express how much I'm grateful to my parents and my wonderful brothers and sister for being the first supporters. I will never forget the support offered by the kind assistant Rana Daragmeh and to all lab friends Lara, Walaa, bayan and Haneen. As we worked as a family and their presence relieved a lot of pressure. Finally, I am eternally grateful to my colleagues, my friends, to everyone who gave me any kind of help and wished me success in my way.

Abstract

Preparation and Characterization of AgO-As_2O_3 Thinfilms

In this thesis, stack layers of oxidized silver and arsenic oxide are fabricated by the thermal evaporation technique under a vacuum pressure of 10^{-5} mbar. Two classes of the films were grown. One is thin (100 nm each sample) and other is thick (1.0 μm) of Ag(O)/As(O). The films are characterized by X-ray diffraction , optical spectrophotometer and impedance spectroscopy techniques, respectively. It was observed that Ag based films are of cubic structure comprising monoclinic AgO as minor phases. The weight of AgO in the films is less than 30%. While the AsO films displayed amorphous nature of structure. The cubic nature of structure is reserved in the Ag(O)/As(O) films. Optically, arsenic oxide films display semiconductor characteristics with energy band gap of 2.41 eV. Coating As oxide onto oxidized Ag films enhanced the light absorbability of As oxide, blue shifts the energy band gap and alters the width of the energy band tails. In addition, the dielectric dispersion in the As oxide films is strongly influenced and decreased in the IR range of light. Modeling of the imaginary part of the dielectric constant using Drude-Lorentz theory allowed determining the optical conductivity parameters. The optical conductivity parameters presented by the drift mobility and Plasmon frequency are suitable for communication technology. The Plasmon frequency reaches 20 GHz which is target in 5G technologies. Electrically, the capacitance-voltage characteristics which were recorded after contacting the films with carbon point contact, revealed metal oxide field effect transistor characteristics. the built in voltage of the device is high enough for the thin film technology. On the other hand, the impedance spectroscopy studies in the frequency domain of 0.01-1.0 GHz have shown that the device could exhibit negative capacitance effect associated with resonance-

antiresonance phenomena in the radio wave and microwave ranges of spectra. These features of the device make it appropriate for communication technologies.

List of Contents

List of Tables

List of Figures

List of Symbols

Symbol	Symbol Meaning
Ag	Silver
As	Arsenic
XRD	X-Ray diffraction
m*	Effective mass
Eg	Energy band gap
Θ	Bragg angle
D	Inter-planner distance
λ	Wavelength
D	Crystallite Size
β	The peak broadening at full width half maximum peak in radians
Δ	Dislocation density
ε	Strain
SEM	Scanning electron microscope
A	Absorption Coefficient
E_e	band tails energy
ε_r	The real part of the dielectric constant
ε_{im}	The imaginary part of the dielectric constant
ω_{pe}	Electron-Plasmon frequency
$\boldsymbol{\varepsilon}_{eff}$	effective dielectric constant
ε_s	The permittivity of semiconductor
T%	Transmittance
R%	Reflectance
ω	Angular frequency

Chapter One

Introduction

Alloys have attracted the attention of research society since decades owing to their wide applications in optics and electronics. As for examples, lead alloy can be employed in electronic devices that are exposed to high temperatures [1]. In another work, the electronic properties presented by band structure, band gap, and density- of- states for $Mo_xW_{1-x}S_2$ alloys are mentioned as promising material for use in transistors and photodetectors [2]. Moreover, the direct band gap nature for alloys gain interest in improving the performance of solar cells such as Si-Ge-Sn or Ge-Sn alloy [3]. In addition, the existence of Se in GSST (Ge-Sb-Se-Te) alloy increases the crystallization temperature and reduce the grain size. In these films, the excess Ge controls the thermal stability of doped alloy [4]. This property make the alloy useful in storage application for automobile systems, this alloy is a choice for high density phase-change memory [4]. Furthermore, $InSe_{0.82}Te_{0.18}$ alloy has a good photoresponse stability and relatively fast response time employed in near infrared range (NIR) photodetector [5]. This alloy displays a broader photoresponse region of 400–1100 nm, because of its smaller direct band gap of 1.13 eV [5].

Many techniques have been used to improve the properties of metals (materials) to form alloys. As for example, Mg alloys are prepared by electrophoretic deposition of alumina/graphene oxide (alumina/GO) coatings [6]. This technique enhanced the tribological, surface mechanical and corrosion properties of Mg alloys [6]. In the same context, Mg alloys are also prepared by grit blasting and laser texturing techniques for thermal spray coating [7]. The coating was distinguished by roughness, porosity and fracture toughness. Laser texturing produced well adhered coatings with adhesion strength of 45.6 MPa [7]. Moreover, The arc-melting method is

utilized to prepare CuNi alloys [8]. The utilization leads to an increase in the strain with increasing concentration of Ni [8]. The CuNi alloys are useful in oil refining and long corrosion free life [8].

Alloys have many important properties. Some of these properties are mechanical properties. As for examples, Mg alloys have a tensile strength of 248.67 MPa and elongation of 3.4% when they are prepared by die casting technique [9]. In addition, nitrogen doped MgZnO ternary alloys have structural and optical properties that are investigated by using Pulsed Laser Deposition technique [10]. In the same context, the concentration of Mg increases as the crystalline quality of MgZnO decreases. The band gap also increases as the nitrogen/oxygen ratio increases from 3.37 to 3.57 eV. Furthermore, the Mg solubility increased by 30% in the alloy, and refractive index had values between 1.7 and 2.0 in visible light range [10].

Alloys based on Ag metal are reported to play important role in many applications due to their mechanical and electrical properties [11]. The addition of Ag on Al alloys increased the tensile strength from 142 MPa to 154 MPa for the Al alloys. It also enhanced the electrical conductivity by about 4% [11]. In addition, Ag-Sn alloys enhanced corrosion resistance and they employed in industrial applications [12]. Ag-Sn alloys are very useful for microelectronics manufacturers [13]. They have many potential advantages, such as low melting point, excellent wetting to common metallic substrates, and enhanced mechanical properties required for microelectronic devices [13]. Moreover, Ti– Zr–Nb–Ta-Ag (TZNT-Ag) alloys are prepared by non-consumable vacuum arc melting and suction casting [14]. The addition of Ag on TZNT alloy increases the resistance and affects the microstructure of the alloy. TZNT-Ag alloys are mentioned employable in biomedical applications [14].

On the other hand, arsenic based alloys are in focus of industry due to the structural, mechanical, electronic and magnetic properties that make them attractive for fabrication of spintronic devices [15]. Antimony-arsenic alloys are another class of alloys which are produced by molecular beam epitaxy [16]. These alloys have physical properties that open the doors to novel applications such as electronic, optoelectronic, quantum, and sensing devices [16]. Moreover, AsP alloys have structural and temperature-dependent transport properties [17]. The existence of high concentration of As forced displaying a metallic behavior of temperature dependent resistance. High concentration of phosphorous in AsP reveals a high thermopower at room temperature [17]. As alloys can be prepared by many techniques. Some of them are the vapor phase transport technique, that used for effective synthesis of AsP alloys [18]. The addition of As on phosphorous established differences in the surface energy between P and As alloy. The surface energy profiles were unusually flat, indicating the variability of the high energy sites on the alloy surface [18].

The above mentioned applications of Ag and As and their smart electrical, structural and mechanical properties, motivated us to prepare Ag(O)/AsO alloys in thin film form. Particularly, in this thesis the structural, electrical and optical properties are investigated. The produced films will be studied by means of X-ray, scanning electron microscopy, ultraviolet visible light spectrophotometer and impedance spectroscopy techniques. This thesis contain an introduction in chapter one, theoretical background in chapter two, experimental details in chapter three, results and discussion in chapter four and conclusion in chapter five.

Chapter Two

Theoretical Background

2.1 The X-ray diffraction

This technique is based on identification of atomic plane orientations defined by the following laws.

2.1.1 Bragg's law

Under constructive interference patterns Bragg's law defined as [19]:

$$2d \sin\theta = n\lambda \tag{2.1}$$

Where d is the distance between two atomic planes and it measured by angstrom. θ is the angle between the incident X-ray beam and the plane surface, n is the integer of the corresponding reflection order and λ is the wavelength of the incident X-ray beam which is equal to 1.5405 Å for Cu anodes.

The structural phases are determined from the measured plane distances using the following equations. For the crystal systems the interplaner spacing is given by :

Triclinic: $a \neq b \neq c, \alpha \neq \beta \neq \gamma \neq 90$

$$\frac{1}{d_{hkl}^2} = \frac{1}{a^2b^2c^2(1-cos^2\alpha-cos^2\beta-cos^2\gamma+2\cos\alpha\cos\beta\cos\gamma}(h^2b^2c^2\,sin^2\alpha$$
$$+k^2a^2c^2sin^2\beta\ +l^2a^2b^2sin^2\gamma\ +2hkabc^2(\cos\alpha\cos\beta-\cos\gamma)$$
$$+2kla^2bc(\cos\beta\cos\gamma-\cos\alpha)+2hlab^2c(\cos\alpha\cos\gamma-\cos\beta)) \quad (2.2)$$

Orthorhombic: $a \neq b \neq c, \alpha = \beta = \gamma = 90$

Equation (2.2) reduced to the formula:

$$\frac{1}{d^2} = \left(\frac{h^2}{a^2}+\frac{k^2}{b^2}+\frac{l^2}{c^2}\right) \quad (2.3)$$

Cubic: $a = b = c, \alpha = \beta = \gamma = 90$

$$\frac{1}{d^2} = \frac{1}{a^2}(h^2+k^2+l^2) \quad (2.4)$$

Impositing the relations between the lattice parameters allow determining the structural formula using equations. There are fourteen configurations of crystal structures that are distributed in seven groups. These structures are called Braves lattices. Table 2.1 shows the fourteen configurations.

Table 2.1: The 14 lattice types in three dimensions.

		primitive	base-centered	centered	face-centered
triclinic		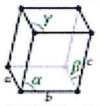			
monoclinic		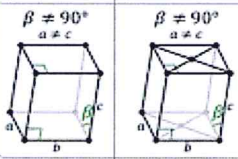			
orthorhombic		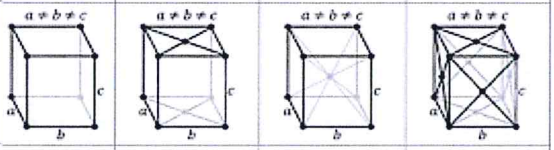			
tetragonal					
hexagonal	rhombohedral	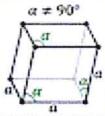			
	hexagonal	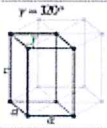			
cubic		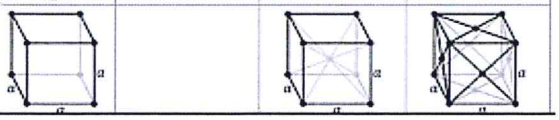			

2.1.2 Structural parameters

The structural parameters of materials can be determined from the most intensive peak which comprises the orientation of most of the crystal planes. The position of the angle and the maximum peak broadening (β) are needed. The structural parameters are presented by:

Strain(ε): is the ratio between the contraction or expansion to the original length [20]:

$$\varepsilon = \frac{\beta}{4\tan(\theta)} \tag{2.5}$$

Crystallite size (D) [20]: accumulation of groups of atoms to form new crystals, it is giving by

$$D = \frac{0.94\,\lambda}{\beta\cos(\theta)} \tag{2.6}$$

Defect density (δ): is a measure of the number of a dislocations in a unit volume of crystalline material [20].

$$\delta = \frac{15\,\varepsilon}{aD} \tag{2.7}$$

Where a is the lattice constant along the a-axis.

Stacking faults (SF) [20]: the number of faults in atomic order.

$$SF = \frac{2\,\pi^2\beta}{45\sqrt{3\tan(\theta)}} \tag{2.8}$$

2.2 Optical properties

The wide variety of the optical properties of the semiconducting materials makes it good candidate martial in opto-electronic applications. Here below some of the important optical properties are listed.

2.2.1 Absorption of Light in Matter

Formulas that are used to explore the optical absorption phenomena in solids :

The absorption coefficient α(hυ) is derived assuming transitions of electrons from an initial state (i) to final state (f). The absorption coefficient takes the form:

$$\alpha(h\upsilon) = A \sum p_{if}\ n_i\ n_f \tag{2.9}$$

Where p_{if} is the probability of electron transition, n_i is the electron density of initial state, n_f is the empty final state density.

Experimentally, the absorption coefficient is determined from Beer's law [21], which expressed by

$$I(z) = I_o e^{-\alpha z} \tag{2.10}$$

The transmittance of light of two parallel surfaces is obtained [22]:

$$T = (1 - R_1)e^{-\alpha d}(1 - R_2) \tag{2.11}$$

Where, $R_1$and R_2 represent the reflectivity's of the film surfaces and d is the medium thickness.

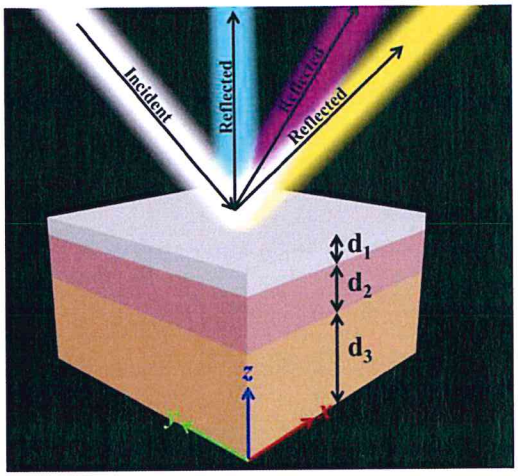

Fig.2.1A light beam incident on an optical medium is exposed to multiple reflections.

When two materials are deposited onto glass, the term (1-R_3) is added to equation (2.11), and transmittance become:

$$T = (1 - R_1)e^{-\alpha d}(1 - R_2)(1 - R_3) \tag{2.12}$$

When $z = d$ the absorption coefficient can be written by:

$$\alpha = -\frac{\ln\left(\frac{T}{(1-R_1)(1-R_2)(1-R_3)}\right)}{d} \tag{2.13}$$

If the reflectance and transmittance are known, the absorbance (A) of a grown film can be determined from:

$$A = -\ln\left(\frac{T}{(1 - R_1)(1 - R_2)}\right) \tag{2.14}$$

where, R_1, R_2 is the reflectance of glass and the sample, respectively.

2.2.2 Band Gap Calculations

The energy band gap is calculated with the help of the Tauc's equation [23] :

$$(\alpha E)^{1/p} = B(E - E_g) \tag{2.15}$$

Where, E is the incident photon energy, p is an index it can have the values 2, 1/2, 3, and 3/2 for indirect allowed, direct allowed, indirect forbidden and direct forbidden electronic transition, respectively. B is a constant that depends on transition probability, and E_g represents the energy gap.

2.2.3 Allowed Direct Transitions

The allowed direct absorption transition occurs when the maximum of the valence band and the minimum of the conduction band have the same value of momentum. The valence band initial states and the conduction band final states are related through the equation [24],

$$E_{cf} = h\upsilon - E_{vi} \tag{2.16}$$

On the other hand, the initial and final states are given by the formulas:

$$E_f - E_g = \frac{\hbar^2 k^2}{2m_e^*} \ , \tag{2.17}$$

and

$$E_i = \frac{\hbar^2 k^2}{2m_h^*} \tag{2.18}$$

When incident photon is interact with solids, the electron is motivated to transfer from the valence band to the conduction band, where:

$$E_{cf} = h\upsilon - |E_{vi}| \tag{2.19}$$

When E_g is subtracted from the both sides of equation and substituting equations (2.17) and (2.18) in the equation (2.19), we get:

$$\frac{\hbar^2 k^2}{2m_e^*} = h\upsilon - E_g - \frac{\hbar^2 k^2}{2m_h^*} \tag{2.20}$$

Rearranging the formula:

$$h\upsilon - E_g = \frac{\hbar^2 k^2}{2m_e^*} + \frac{\hbar^2 k^2}{2m_h^*} = \frac{\hbar^2 k^2}{2}\left(\frac{1}{m_e^*} + \frac{1}{m_h^*}\right) \tag{2.21}$$

rearranging equation (2.21), yields:

$$k^2 = \frac{2(h\upsilon - E_g)}{\hbar^2} m_r \tag{2.22}$$

m_r is the reduced effective mass, where ${m_r}^{-1} = \frac{1}{m_e^*} +$

$\frac{1}{m_h^*}$ (2.23)

The density of state in an energy range has the following formula:

$$N(h\upsilon)d(h\upsilon) = \frac{8\pi k^2 dk}{(2\pi)^3} \tag{2.24}$$

By differentiate equation (2.22) with respect to k *and* $h\upsilon$, respectively. The equation become:

$$2kdk = \frac{2m_r}{\hbar^2} d(h\upsilon) \tag{2.25}$$

By substituting equations (2.22) and (2.25) in (2.24), the density of states become:

$$N(h\upsilon)d(h\upsilon) = \frac{16\pi(h\upsilon - E_g)m_r}{\hbar^2(2\pi)^3} dk \tag{2.26}$$

Simplifying equation (2.26), by substituting equations (2.22)and (2.25) in it, the density of states equation will be rewritten as,

$$N(h\upsilon)d(h\upsilon) = \frac{16\pi(h\upsilon - E_g)}{\hbar^2(2\pi)^3} \frac{m_r^2}{\hbar^2\sqrt{\frac{2(h\upsilon - E_g)m_r}{\hbar^2}}}\, d(h\upsilon) \qquad (2.27)$$

This equation is then simplified to take the form,

$$N(h\upsilon)d(h\upsilon) = \frac{(2m_r)^{\frac{3}{2}}}{2\pi^2\hbar^3}(h\upsilon - E_g)^{\frac{1}{2}}\, d(h\upsilon) \qquad (2.28)$$

The absorption coefficient is linearly proportional to the initial $N_i$and final N_f states as follow,

$$\alpha(h\upsilon) = A^*(h\upsilon - E_g)^{\frac{1}{2}} \qquad (2.29)$$

Where,

$$A^* = \frac{q^2(\frac{2m_h^* m_e^*}{m_h^* + m_e^*})^{\frac{1}{2}}}{nch^2 m_e^*} \qquad (2.30)$$

2.2.4 Forbidden Direct Transitions

In this case, the initial and final states have total angular momentum equal to zero. The probability of the forbidden transition directly proportional to k^2. The forbidden direct transition will contain an extra$(h\upsilon - E_g)$ [24]. Thus, the forbidden direct transition absorption coefficient is given by :

$$\alpha(h\upsilon) = A'(h\upsilon - E_g)^{\frac{3}{2}} \qquad (2.31)$$

Fig. 2.2 represents the (a) direct and (b) indirect band gap transition.

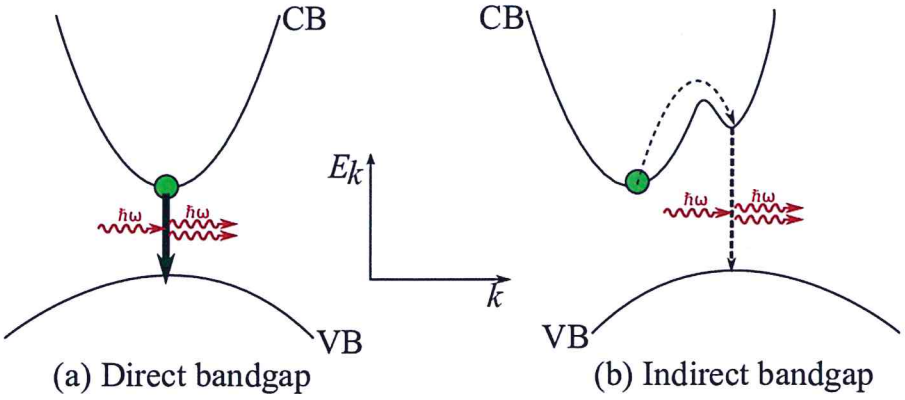

Figure 2.2: The (a) direct and (b) indirect transitions.

2.2.5 Indirect Valleys and Indirect Transitions

The indirect band gap is a band gap with indirect transitions. The indirect band gap is formed between the minimum energy of the conduction band and the maximum energy of the valence band that occurs at a different k values [24]. Therefore, a phonon is either absorbed or emitted in order to consummate an indirect electron transition from valence to the conduction band.

$$h\upsilon_c = E_f - E_i + E_p \tag{2.32}$$

$$h\upsilon_a = E_f - E_i - E_p \tag{2.33}$$

2.2.6 Urbach Band Tails

Band tails are localized electronic states that existed below the conduction band (CB) or above the valence band (VB), the band tails arise as a consequence of disorder [25]. The density of initial state is proportional to the square root of the valence band $E_v^{1/2}$ .The band tails density of states is presented by,

$$N_f = N_o e^{E/E_o} \tag{2.34}$$

Using this relation we can calculate the absorption coefficient which is expressed as follows,

$$\alpha(hv) = A\int_{E_v}^{hv-E_v} |E_v|^{1/2}\, e^{E/E_o} dE \tag{2.35}$$

Solve the integration by changing variables we indicate:

$$\alpha(hv) = -Ae^{hv/E_o}(E_o)^{3/2}\int_{\frac{hv+E_v}{E_o}}^{\frac{E_v}{E_o}} x^{1/2}\, e^{-x} dx \tag{2.36}$$

Set the lower limit in integration ∞ and divide the integral into two periods $(\infty - 0) and \left(0 - \frac{E_v}{E_o}\right)$. We get,

$$\alpha(hv) = A(E_o)^{3/2} e^{hv/E_o}\left(\frac{1}{2}\pi^{1/2} - \int_0^{\frac{E_v}{E_o}} x^{1/2}\, e^{-x} dx\right) \tag{2.37}$$

If the semi logarithmic plot is drawn the slope of that figure is indicates that the width of band tails can be expressed by:

$$E_o = \left(\frac{d\, ln\alpha}{d\, hv}\right)^{-1} \tag{2.38}$$

Or,

$$\frac{1}{E_o} = \frac{d\ln(\alpha)}{d(hv)} \tag{2.39}$$

$$\frac{1}{E_o} d(hv) = d\ln(\alpha) \tag{2.40}$$

Integrating and take the exponential of both sides, we get:

$$\alpha = \alpha_o e^{E/E_o} \tag{2.41}$$

2.2.7 Refractive index and dielectric constant

Refractive index of material is a dimensionless number which describes how fast is the light propagate through the material. It is a complex number consists real and imaginary parts. The relation between the refractive index and the optical wavelength is introduced by an equation called the dispersion equation [26]. The dispersive refractive index can be written as,

$$N_{complex} = n(\lambda) + iK(\lambda)$$

$$= (\varepsilon_r + i\varepsilon_{im})^{1/2} \tag{2.42}$$

$K(\lambda)$ is the extinction coefficient, while ε_r and ε_{im} is the real and imaginary dielectric constants, respectively.

The effective dielectric constant ε_{eff} can be expressed in terms of real and imaginary dielectric constants as follows.

$$\varepsilon_{eff} = \varepsilon_r + i\varepsilon_{im} \tag{2.43}$$

The effective dielectric constant ε_{eff} is expressed also in terms of the refractive index $n(\lambda)$:

$$\varepsilon_{eff} = n^2(\lambda) \tag{2.44}$$

By squaring the equation (2.42) we get the following relation:

$$n^2(\lambda) - k^2(\lambda) + i2n(\lambda)K(\lambda) = \varepsilon_r + i\varepsilon_{im} \tag{2.45}$$

By comparing the real and imaginary parts on both sides of equation (2.41), We can get ε_r and ε_{im} in terms of $n(\lambda)$ and $K(\lambda)$:

$$n^2(\lambda) - k^2(\lambda) = \varepsilon_r \tag{2.46}$$

$$2n(\lambda)K(\lambda) = \varepsilon_{im} \tag{2.47}$$

By substituting $n^2(\lambda)$ by ε_{eff} in (2.46) and $(\varepsilon_{eff})^{1/2}$ in (2.47), we get:

$$\varepsilon_r = \varepsilon_{eff} - \left(\frac{\alpha\lambda}{4\pi}\right)^2 \tag{2.48}$$

$$\varepsilon_{im} = 2\,(\varepsilon_{eff})^{1/2}\frac{\alpha\lambda}{4\pi} \tag{2.49}$$

The normal reflectance and the reflection coefficient is given by,

$$R = \left|\frac{E_2}{E_1}\right|^2 \tag{2.50}$$

$$r = \frac{E_2}{E_1} \tag{2.51}$$

, respectively. Where

$$E_1 = \frac{1}{2}E_o\left(1 + N_{complex}\right) \tag{2.52}$$

$$E_2 = \frac{1}{2}E_o\left(1 - N_{complex}\right) \tag{2.53}$$

E_1 and E_2 expressed the electric field along the z-axis.

Substitute (2.52) and (2.53) in (2.50) and rewrite the equation in terms of $N_{complex}$,

$$R = \left|\frac{1 - N_{complex}}{1 + N_{complex}}\right|^2 = \frac{(1-n)^2 + k^2}{(1+n)^2 + k^2} \tag{2.54}$$

The reflectance $R\ in$ the terms of effective dielectric constant ε_{eff} can be expressed by the following relation:

$$R = \frac{(\sqrt{\varepsilon_{eff}} - 1)^2 + k^2}{(\sqrt{\varepsilon_{eff}} + 1)^2 + k^2} \tag{2.55}$$

Where,

$$k = \frac{\alpha\lambda}{4\pi} \tag{2.56}$$

We can rewrite equation (2.55) to extract ε_{eff} as a function of the light reflectance R.

$$R(\sqrt{\varepsilon_{eff}} + 1)^2 + Rk^2 = (\sqrt{\varepsilon_{eff}} - 1)^2 + k^2 \tag{2.57}$$

By following some steps we get the expression:

$$\varepsilon_{eff} + \frac{2(R+1)}{R-1}\sqrt{\varepsilon_{eff}} + k^2 = 0 \tag{2.58}$$

Equation (2.58) represents a quadratic relations that indicates two roots:

$$\varepsilon_{eff1} = \left(\frac{-2\frac{(R+1)}{(R-1)} + \sqrt{4\frac{(R+1)^2}{(R-1)^2} - 4k^2}}{2}\right)^2 \tag{2.59}$$

$$\varepsilon_{eff2} = \left(\frac{-2\frac{(R+1)}{(R-1)} - \sqrt{4\frac{(R+1)^2}{(R-1)^2} - 4k^2}}{2}\right)^2 \quad (2.60)$$

2.2.8 Drude-Lorentz Model

The imaginary dielectric constant spectra ε_{img}can be analyzed using the effective oscillator model. Dielectric solid atoms or molecules can be treated as a agglomerate of oscillators. As the oscillations of a free electron induced by AC electric fields $E(t)$ of a light wave polarized along the x-axis. The equation of motion that describes the electron motion is expressed by,

$$m_o \frac{d^2x}{dt^2} + m_o\gamma\frac{dx}{dt} + m_o\omega_o^2 x = -eE \quad (2.61)$$

Where, m_o is the electron mass, x is the electron displacement, γ is the damping coefficient, e is the electron charge and E is the electric field. The electric field can expressed by:

$$E(t) = E_o\cos(\omega t + \varphi) = E_o\mathrm{Re}\left(e^{-i\omega t-\varphi}\right) \quad (2.62)$$

The AC electric field brings on oscillations can be written as

$$X(t) = X_o\mathrm{Re}\left(e^{-i\omega t-\varphi\prime}\right) \quad (2.63)$$

Where, X_o is the amplitude of the electron displacement and φ' is the phase of oscillation. To find X_o, the first and second derivative of the electron displacement were found, and were inserted to the equation of motion (2.61). Then the final formula take the form:

$$X_o(-\omega^2 + \gamma(-i\omega) + \omega_o^2) = -\frac{e}{m_o}E_o \quad (2.64)$$

$$X_o = -\frac{\frac{e}{m_o}E_o}{(\omega_o^2 - \omega^2 - i\gamma\omega)}, \quad (2.65)$$

the displacement vector takes the form,

$$X(t) = -\frac{\frac{e}{m_o}E_o}{(\omega_o^2 - \omega^2 - i\gamma\omega)}\left(e^{-i\omega t}\right) \tag{2.66}$$

The electric displacement D of a solid counts on the electric field and polarization as follows.

$$D = \varepsilon_o E + p \tag{2.67}$$

Where,

$$p_{resonant} = \frac{Ne^2}{m_o}\frac{1}{\omega_o^2 - \omega^2 - i\gamma\omega}E \tag{2.68}$$

the electric displacement can be redefined as

$$D = \varepsilon_o \varepsilon_r E \tag{2.69}$$

Where, ε_r is the relative dielectric constant.

And the electric displacement for resonant and non-resonant can be defined as

$$\begin{aligned} D &= \varepsilon_o E + p_{background} + p_{resonant} \\ &= \varepsilon_o E + \varepsilon_o \chi E \\ &\quad + p_{resonant} \end{aligned} \tag{2.70}$$

Where

$$p_{resonant} = Np = -Nex \tag{2.71}$$

Then, the relative dielectric constant takes the form

$$\varepsilon_r(\omega) = 1 + \chi + \frac{Ne^2}{\varepsilon_o m_o}\left(\frac{1}{\omega_o^2 - \omega^2 - i\gamma\omega}\right) \tag{2.72}$$

By separating the equation into real and imaginary dielectric constants $\varepsilon_1$and ε_2 :

$$\varepsilon_1(\omega) = 1 + \chi + \frac{Ne^2}{\varepsilon_o m_o}\left(\frac{\omega_o - \omega^2}{(\omega_o^2 - \omega^2)^2 + (\gamma\omega)^2}\right) \tag{2.73}$$

$$\varepsilon_2(\omega) = \frac{Ne^2}{\varepsilon_o m_o}\left(\frac{\gamma\omega}{(\omega_o^2 - \omega^2)^2 + (\gamma\omega)^2}\right) \tag{2.74}$$

The relative dielectric constant ε_r at $\omega = 0$ represent the static dielectric constant ε_{st}.

In the low frequency material permittivity

$$\varepsilon_1(0) = \varepsilon_{st} = 1 + \chi + \frac{Ne^2}{\varepsilon_o m_o \omega_o^2} \tag{2.75}$$

The high frequency permittivity can be indicated by the relative dielectric constant at $\omega = \infty$,

$$\varepsilon_r(\infty) = \varepsilon_\infty = 1 + \chi \tag{2.76}$$

2.3 Impedance Spectroscopy

Through measuring the impedance spectroscopy, Impedance takes the following form,

$$Z = \frac{V}{I}(\Omega's) \tag{2.77}$$

Considering series RLC circuits consist of a resistance, a capacitance and an inductance connected in series across an alternating current supply as shown in Fig. 2.3, one find,

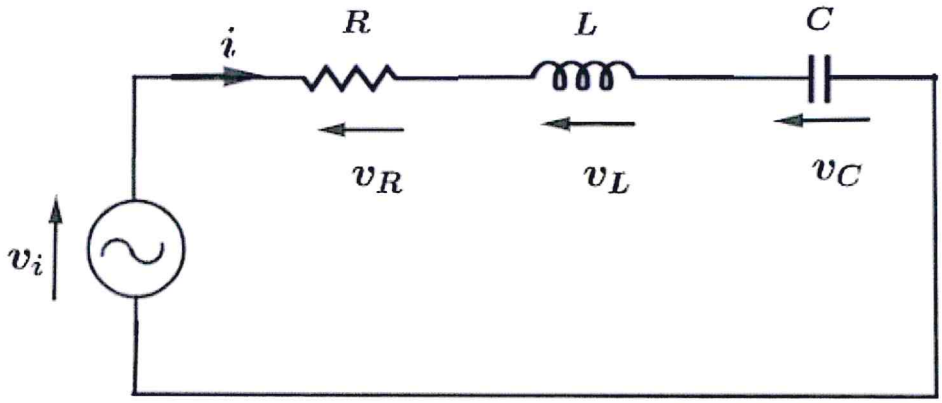

Figure 2.3: The RLC circuit.

$$V_i = V_0 e^{i\omega t} \quad (2.78)$$

V_R

$$= IR \quad (2.79)$$

$$V_L = I\omega L \quad (2.80)$$

$$V_C = \frac{I}{\omega C} \quad (2.81)$$

Employing Kirchhoff's voltage law (KVL)

$$V_i - V_R - V_L - V_C = 0 \quad (2.82)$$

$$V_i = IR + I\omega L + \frac{I}{\omega C} \quad (2.83)$$

The voltage triangle for a series RLC circuit as Fig.2.4 show, take the form:

$$V_S = ({V_R}^2 + ((V_L - V_C)^2)^{1/2} \quad (2.84)$$

substituting the values of V_R, V_L, V_C in (2.83) give:

$$V_S = ((IR)^2 + (IX_L - IX_C)^2)^{1/2} \quad (2.85)$$

$$V_S = I \times Z \tag{2.86}$$

Where:

$$Z = (R^2 + (X_L - X_C)^2)^{1/2} \tag{2.87}$$

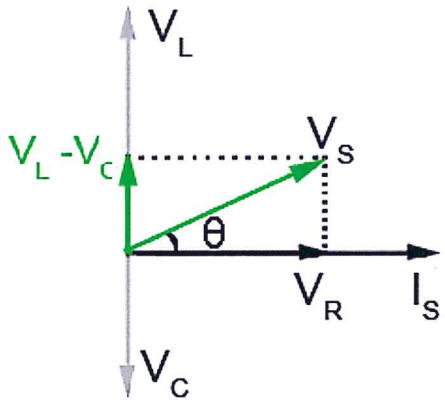

Figure 2.4: The voltage triangle of a series RLC circuit

Chapter Three

Experimental Details

3.1: Glass Cleaning:

Glass slides of dimensions 2.54×7.62 cm were cleaned by using distilled water and alcohol. The cleaned glass slides were inserted into a beaker that is filled with alcohol. The beaker was covered by aluminum foil and put onto the heater for 15 minutes until the temperature reached 70 °C. In order to remove the dust and the proteins existing on the surface. The glass slides were ultrasonically cleaned for 40 minutes at temperature of 70 °C after they were immersed in the alcohol. The glass slides were taken out from the ultrasonic device and used as substrate for the evaporation of the films.

3.2: Thin/Thick Films preparation:

The high purity silver powder is used as source material to produce Ag(O) thin films. A weight of 0.5 gm of Ag powder was used. The 100 nm thickness of Ag films are deposited onto ultrasonically cleaned glasses by thermal evaporation technique using VCM 600 physical vapor deposition system (Fig. 3.1) under the vacuum pressure of 5×10^{-5} mbar. During the evaporation process, the film thickness was monitored via thickness monitor located in the chamber that is connected to a quartz crystal. The resulting Ag(O) thin films was re-used as a substrate for the evaporation of the arsenic (oxide) layer to prepare Ag(O)/As(O) films. A 0.5 gm of arsenic (oxide) lumps was used in this run. The recorded thickness of As(O) was on the order of 100 nm. The prepared Ag(O)/As(O) thin film has a thickness of 200 nm.

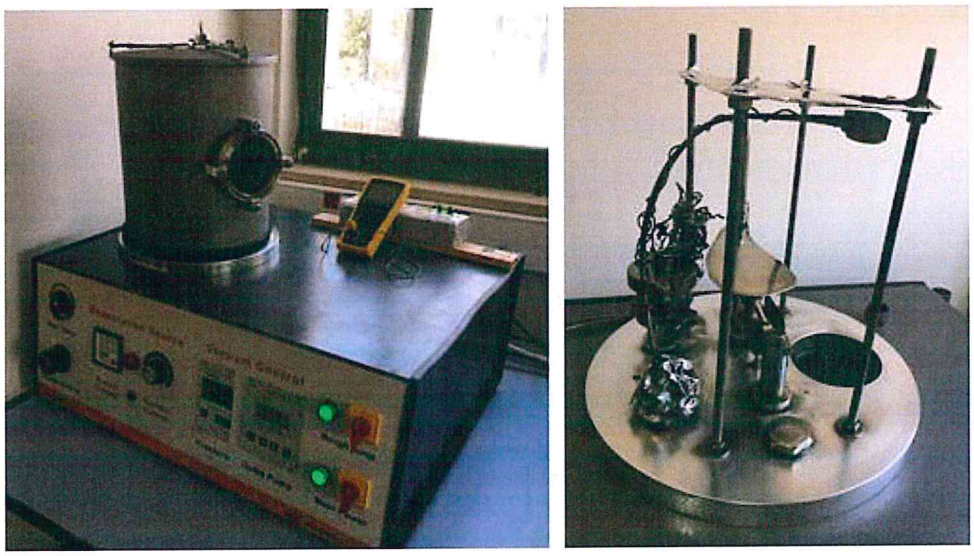

Figure 3.1: The VCM 600 evaporation system.

On the other hand, a weight of 0.6 gm of Ag powder was used to get thick films by using the evaporation system shown in figure 3.1. A 1 μm thick Ag(O) films were grown. Some of the Ag(O) films were used as a substrate to deposit arsenic thick films. Here, a 0.6 gm of arsenic

lumps were used as evaporation source to grow As(O) films of thickness of 1 μm. The thickness of 1 μm of the arsenic oxide films was prepared by evaporation technique.

The thickness of the Ag(O), As(O), Ag(O)/As(O) thin/thick films was measured by high-resolution 106 Inficon STM-2 thickness monitor, respectively. The measured values are confirmed by surface roughness tester-profilometer (Model SOLID TR-200 plus). The profilometer reads an average of ~124 nm, 120 nm and 244 nm for Ag(O), As(O) and Ag(O)/As(O) thin films, respectively, and an average of ~823 nm, 1 μm and 1.823 μm for Ag(O), As(O) and Ag(O)/As(O) thick films, respectively. Fig. 3.2 shows the surface roughness tester.

Figure 3.2: The surface roughness profilometer (Model SOLID TR-200 plus) system.

The geometrical design and the optical images of the films are shown in Fig. 3.3 and Fig. 3.4 below.

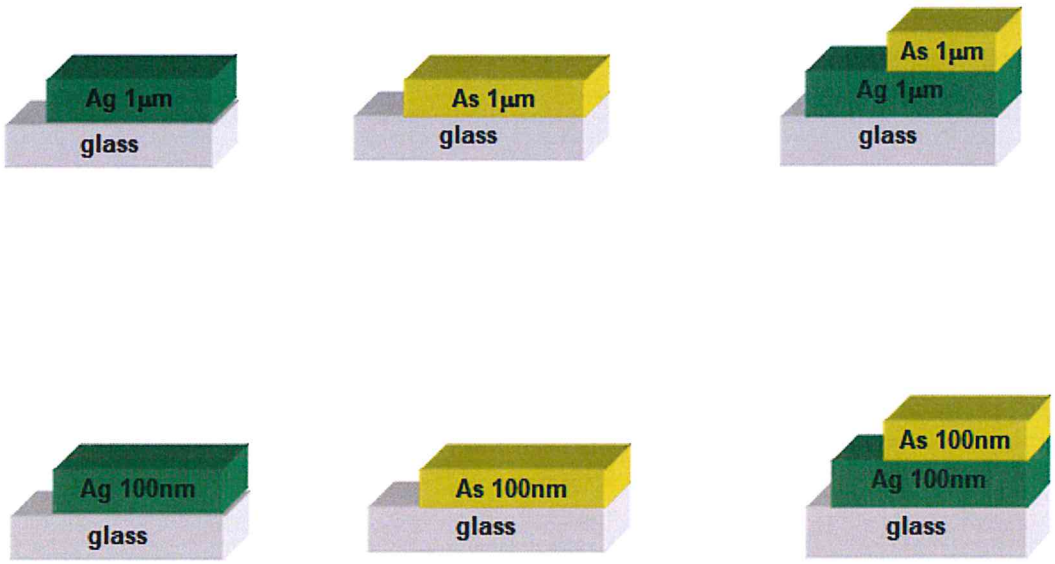

Figure 3.3: The geometrical design of the Ag(O), As(O), Ag(O)/As(O) thick/thin films.

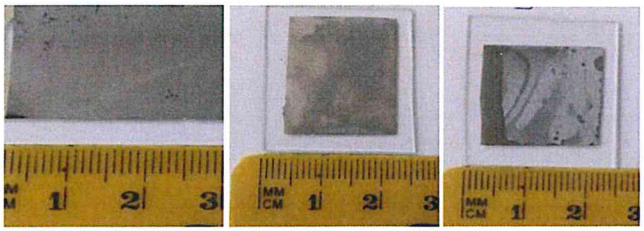

Glass/Ag(O) Glass/As(O) Ag(O)/As(O)

Figure 3.4: the optical images of the grown films of Ag(O), As(O), Ag(O)/As(O).

3.3: Thin/Thick Film Analysis:

The prepared films were subjected to different measuring techniques in order to investigate their conductivity type, optical, structural and electrical properties. The hot probe technique, optical spectrophotometer, X-ray diffraction analysis and impedance spectroscopy measurements for the studied samples are explained in the following sections.

3.3.1: The Hot Probe Technique:

The hot probe technique which is illustrated in Fig. 3.5 is used to check the conductivity type (n-type or p-type) of the studied samples. This method consists of a hot probe and a standard digital multimeter that allows the identification of conduction type of semiconductors. The experiment is carried out by heating the soldering iron for a short period. The hot probe was connected to the positive side of the multimeter. Whereas, the cold probe was connected to the negative side. When the voltage reading were varied from positive to the negative, the type of semiconductor is p-type. While, the positive reading of voltage on the multimeter give a n-type semiconductor.

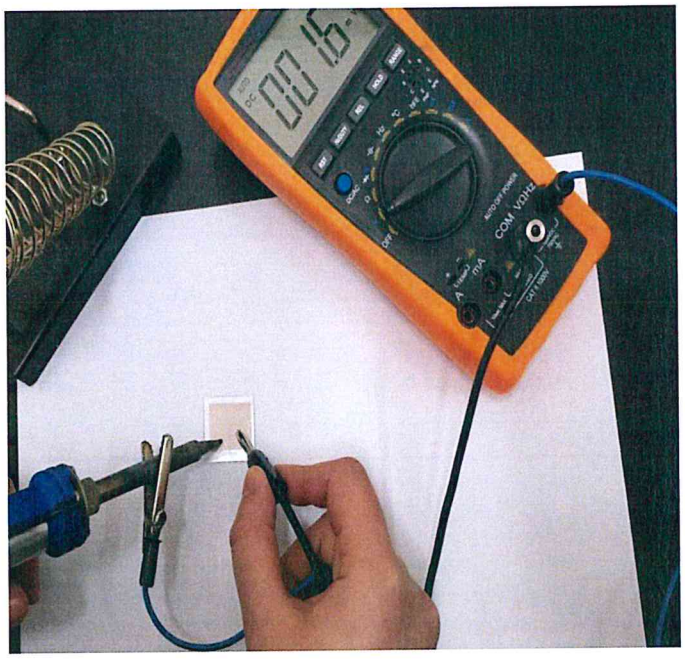

Figure 3.5: The set up of hot probe technique.

3.3.2: X-ray Diffraction (XRD) Measurements:

The Ag(O), As(O), Ag(O)/As(O) thin/thick films and arsenic oxide bulk are structurally characterized by Rigaku MiniFlex-600 X-ray diffraction unit. The Rigaku MiniFlex-600 X-ray diffraction unit is displayed in Fig. 3.6. X-ray were provided from Kα radiation of a copper anode of wavelength of 1.5405 Å. XRD patterns were recorded at a scan speed of 1°/min, and diffraction angle range of 2θ being 10°-70°. The diffraction patterns were analyzed by employing the Bragg's diffraction law $\lambda = 2d \sin\theta$, where λ is the wavelength of the x-ray which is 1.5405 Å, d is the distance between oriented planes and 2θ is the positions of the diffraction peaks. The

analysis of the diffraction patterns were analyzed with the help of TREOR 92 and crystal diffraction software packages.

Figure 3.6: X-ray Rigaku diffractometer.

3.3.3: Optical Measurements:

The optical transmittance and reflectance spectra were measured with the help of Thermoscientific Evolution 300 ultraviolet–visible light spectrophotometer in the spectral range of 190-1100 nm. Pike technology reflectometer was used to measure the reflectance at normal incidence. The device is equipped with a xenon (Xe) lamp that emits light at different frequencies. The measurements were carried out at scanning speed of 1200 nm/min. The vision

pro program was used to analyze the measured data. The Thermoscientific Evolution 300 ultraviolet–visible light spectrophotometer is presented in Fig. 3.7.

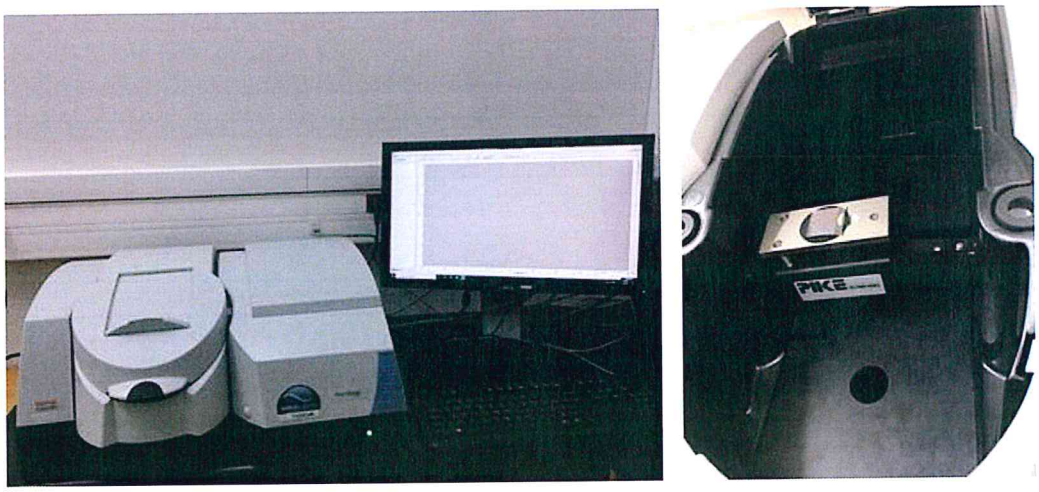

Figure 3.7: The UV-VIS spectrophotometer.

3.3.4: Impedance Measurements

For purpose of electrical measurements a carbon point contact of area of 0.0314 cm^2 was painted onto As(O) layer surface. The impedance spectroscopy measurements of Ag(O)/As(O)/C device were carried out with the help of the Agilent 4291B 0.01–1.80 GHz impedance analyzer. The impedance, capacitance, conductance and reflection coefficient were measured in the frequency range of 0.01-1.80 GHz. The data was collected with the help of MATLAB software packages. The capacitance-voltage measurements for the Ag(O)/As(O)/C were recorded at signal frequency of 1 MHz under nobiasing voltage (V=0 volt). The impedance analyzer system which is displayed in Fig. 3.8 is equipped with the Agilant material analyzer that is shown in Fig 3.8(b).

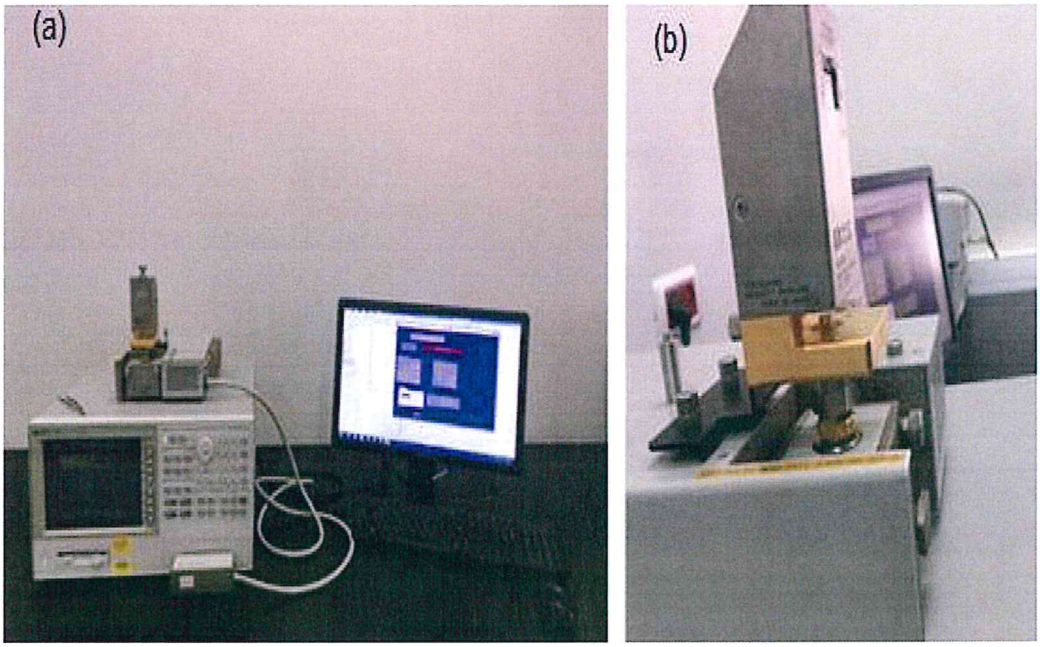

Figure 3.8: The Agilent 4291B 0.01–1.80 GHz impedance analyzer.

Chapter Four

Results and Discussion

4.1: Analysis of the X-ray diffraction technique:

4.1.1: Formation of Ag(O)/As(O) alloys

Stacked layer of Ag(O)/As(O) films were prepared by the thermal evaporation technique. Thin films of total thickness of 200 nm are named "thin" and used for optical measurements as they are partially transparent. Thick films of 2 μm are named "thick" and used for electrical measurements. The X-ray diffraction (XRD) patterns which resulted from vaporization of arsenic onto silver are illustrated in Fig 4.1. The data is measured for the thick films.

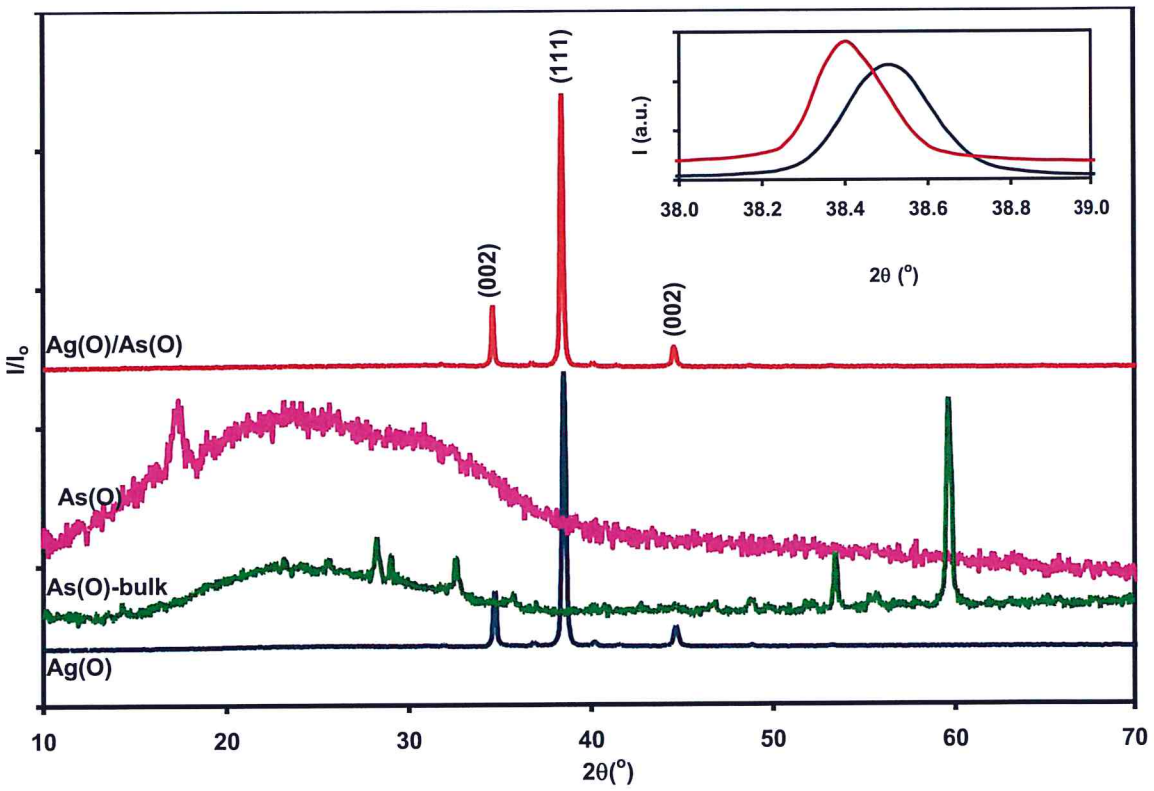

Figure 4.1 The X-ray diffraction patterns for Ag(O), As(O), Ag(O)/As(O) thick films and As bulk. The inset shows the variation of the maximum peak intensity with 2θ.

The intensive peaks of XRD patterns are analyzed with help of the "TREOR 92" software packages. By using "TREOR 92" all possible structures were taken into account. Acceptance or rejection of the theoretically obtained crystal structure is based on the value of the 2θ differences between observed and calculated 2θ values. The "TREOR 92" software packages can obtain the

miller indices (hkl) and the lattice parameters of a particular structure. It can also specify the appropriate crystal structure. In the evaluation process, the observed 2θ values and respective intensities are given as an input to the software. Then, a typical crystal structures is selected. The obtained solution is associated with guessed lattice parameter 2θ values and Δ2θ. For our samples, the percentage error (Δ2θ %) being less than 2% were restricted to accept the diffraction angle position otherwise it is rejected.

Table 4.1 illustrated the structural phases for the Ag thin films. The table displayed the experimental 2θ values and intensity at room temperature. It also shows the values of particular structural percentage Δ2θ % by taking least differences between the seven structures. It obvious that the Ag(O) has more than one structure.

Initial tests on the XRD patterns obtained from "TRIOR 92" Ag films indicated that the peaks centered at 38.5°, 44.65°, 64.75° are indexed assuming a cubic cell with lattice parameters $a = b = c = 4.05$ Å. The data is consistent with the reported literature data for Ag films. To identify the other peaks, tests were carried out by inserting the lattice parameters for cubic Ag_2O ($a = b = c = 4.718$ Å, Pn3m). None of the observed peaks can be assigned to Ag_2O. The same were also repeated for monoclinic AgO ($a = 5.85$ Å, $b = 3.47$ Å, $c = 5.49$ Å, $\beta = 107.3°$, p21/c). The experimentally observed peaks other than the cubic ones, we correctly indexed for monoclinic AgO phase. Hence, the Ag films are composed of cubic Ag metal and monoclinic AgO. The miller indicies are shown in Table 4.1. Calculations of the phase weights have shown that the films are composed of 71.1% Ag and 28.9% AgO.

Table 4.1: The XRD reflections analysis for the Ag thick film.

Observed 2θ	Cubic Ag	Monoclinic AgO

31.05	-	2 0 $\bar{1}$
31.95	-	2 0 0
34.70	-	0 0 2
38.50	1 1 1	-
40.20	-	2 0 1
44.65	0 0 2	-
48.90	-	3 0 0
53.25	-	2 0 $\bar{3}$
64.75	0 2 2	-
69.00	-	2 2 1

On the other hand, as can be seen from Fig. 4.1, the x-ray diffraction patterns for the arsenic oxide film displays no intensive peaks. As a result, the arsenic has an amorphous nature when coated onto glass substrate. However, the XRD for bulk form of arsenic oxide that are illustrated in Fig 4.1 displayed many peaks, the sharpest one is located at 2θ of 59.65° diffraction angle. The XRD patterns are resolved by the help of "TREOR 92" software packages through entering the values of 2θ and their intensities. By this method, we get the solution via comparing the differences between the experimentally observed and theoretical values of 2θ. If the percent difference less than 2% is taken other than that it is refused.

Table 4.2. The XRD reflections analysis for the arsenic bulk.

2θ	I (c/s)	I/Io	Hkl
25.65	1311	0.43	0 0 3
28.20	1486	0.49	-
29.05	1337	0.44	0 1 -1
32.65	1292	0.43	0 1 2
35.75	913	0.30	-

46.85	835	0.28	-
48.90	846	0.28	1 1 0
51.90	816	0.27	0 1 5
52.20	832	0.27	0 0 6
55.65	893	0.29	1 1 3
55.70	902	0.30	1 1 3
59.65	3035	1.00	0 2 -2

The X-ray analysis for the arsenic oxide bulk is presented in Table 4.2 Fourteen peaks are observed. The peak analysis which is executed with the help of "TREOR 92" software packages showed that the bulk is mostly of trigonal arsenic ($a = b = 3.759$ Å$, c = 10.578$ Å$, \gamma = 120°, R - 3m$) and cubic As_2O_3 ($a = b = c = 11.0457$ Å, $Fd3m$). Calculations of the phase weights have shown that the films are combined of 67.5% As and 32.5% As_2O_3.

Furthermore, the x-ray diffraction patterns for Ag(O)/As(O) thick films are represented in fig 4.1. As seen from the figure the appearance of the intensive peaks in the XRD of the glass/Ag(O)/As(O) films are accepted to be of polycrystalline nature. As the figure show, the maximum peak become stronger and sharper than the Ag-film. The XRD patterns are analyzed by "TREOR 92" software packages. The analysis shows the effect of arsenic oxide on the structure of Ag-film. Most of the observed peaks are index and assigned to Ag metal, peaks of As(O) did not appear, nor those of AgO. All the observed peaks are shifted toward lower different angles. In addition, the new peak which is observed at 2θ=40 can be assigned to As_2O_3. The existence of the oxidized phases (AgO, As_2O_3) probably resulted from exposing the films to air during the replacement of the evaporation of Ag by arsenic.

In order to reveal the effects of arsenic on the structural properties of Ag-film, the maximum peak which was observed at 38.5° and oriented in the (111) orientation direction was taken into

account. As the inset of figure 4.1 illustrates, the diffraction peaks shifted toward smaller diffraction angles. Particularly, the maximum peak position shifted from $2\theta = 38.5^{o}$ to 38.4^{o}. The intensity values increased from 45997 c/s to 50065 c/s. In addition, it is also noticed that the maximum peak become narrower indicating improvement in the crystallinity.

Table 4.3 shows some of the structural parameters including crystallite size (D), strain (ε), dislocation density (δ) and stacking faults (SF%). The structural parameters are determined from major peak and 2θ values with the help of the previously mentioned relations (in theoretical part). The crystallite size of Ag-films exhibited a value of 35 nm. It is increased as the arsenic was coated onto Ag-films reaching a value of 44 nm. The increase in crystallite size is due to enhanced dynamical recrystallization or reduced strain [27]. On the other hand, the lattice strain shows an opposite trend of variations. ε decreased from 3.124×10^{-3} to 2.506×10^{-3} when arsenic oxide grew on Ag(O)-films. The reduction in micro strain is assigned to the completed bonding and decreasing stacking fault concentrations [28]. The calculated dislocation density for Ag-film shows a value of 3.291×10^{14} lines/cm^2. It decreased to reach a value of 2.107×10^{14} lines/cm^2 when coated with As(O). The same behavior are observed for stacking faults. Specifically, the stacking faults percentage decreased upon coating of arsenic on Ag-films to reach a value of 0.150%.

Table 4.3: The structural parameters for Ag(O) and Ag(O)/As(O) films.

Sample	D(nm)	$\varepsilon\times10^{-3}$	SF%	δ(a)$\times10^{14}$(line/cm^2)	δ(b)$\times10^{14}$(line/cm^2)	δ(c)$\times10^{14}$(line/cm^2)
Ag(O)	35	3.124	0.187	3.291	3.291	3.291
Ag(O)/As(O) fresh	44	2.506	0.15	2.107	2.107	2.107

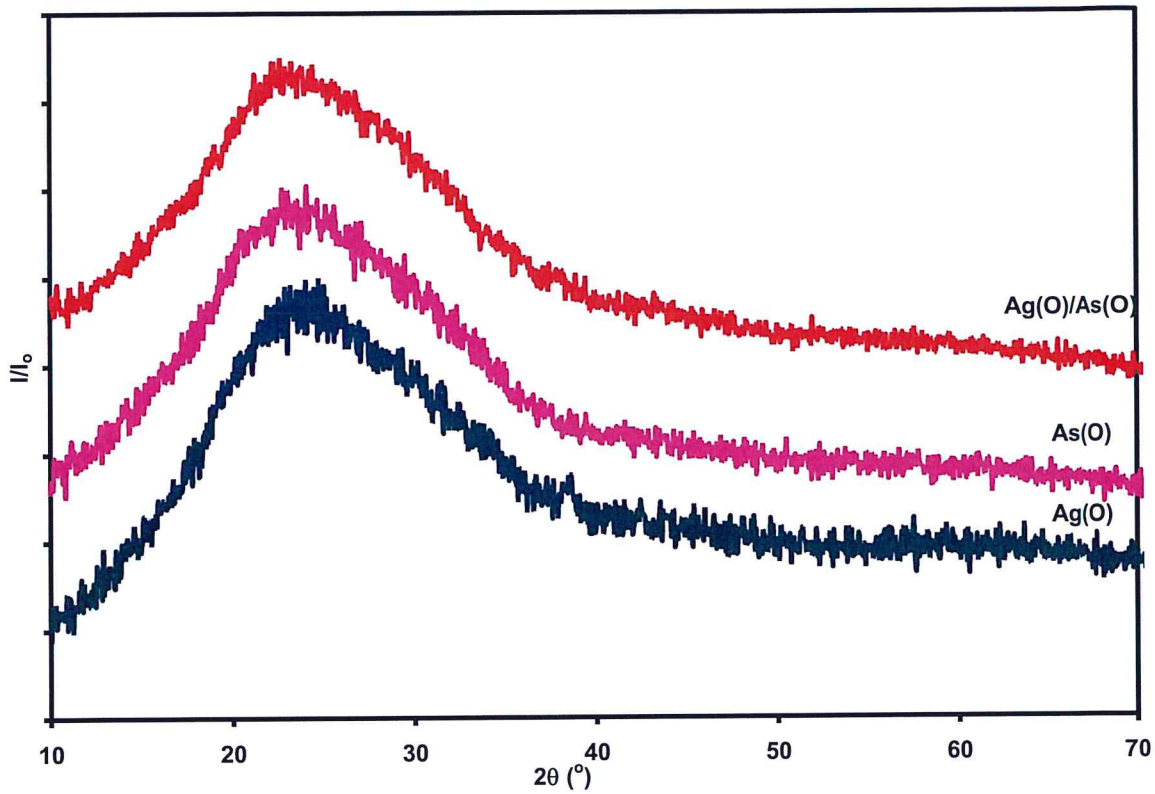

Figure 4.2 The X-ray diffraction patterns for Ag(O), As(O) and Ag(O)/As(O) thin films.

The x-ray diffraction patterns (XRD) of the Ag(O), As(O) and Ag(O)/As(O) thin films are shown in Fig. 4.2. As a result of appearance of no intensive peaks in the XRD for glass/Ag, glass/As and glass/Ag/As thin films, respectively. The samples are accepted to be of amorphous nature when coated onto glass substrates. All observed films are of amorphous nature due to the absence of sharp peaks [29], structural defects and band tails [30].

4.1.2 Energy-Dispersive X-ray Spectroscopy (EDS):

We have measured different areas on the sample surface. The image in Fig 4.3 show the energy dispersive X-ray spectroscopy for Ag(O)/As(O) thick film of thickness of 2 μm for one of the

areas. In the selected area four regions were selected, one is the white region, another is the mixed region containing black colored and white colored points, the third is white petite and the fourth is moderate. The EDS spectra which were taken from different points is shown in Fig. 4.4.

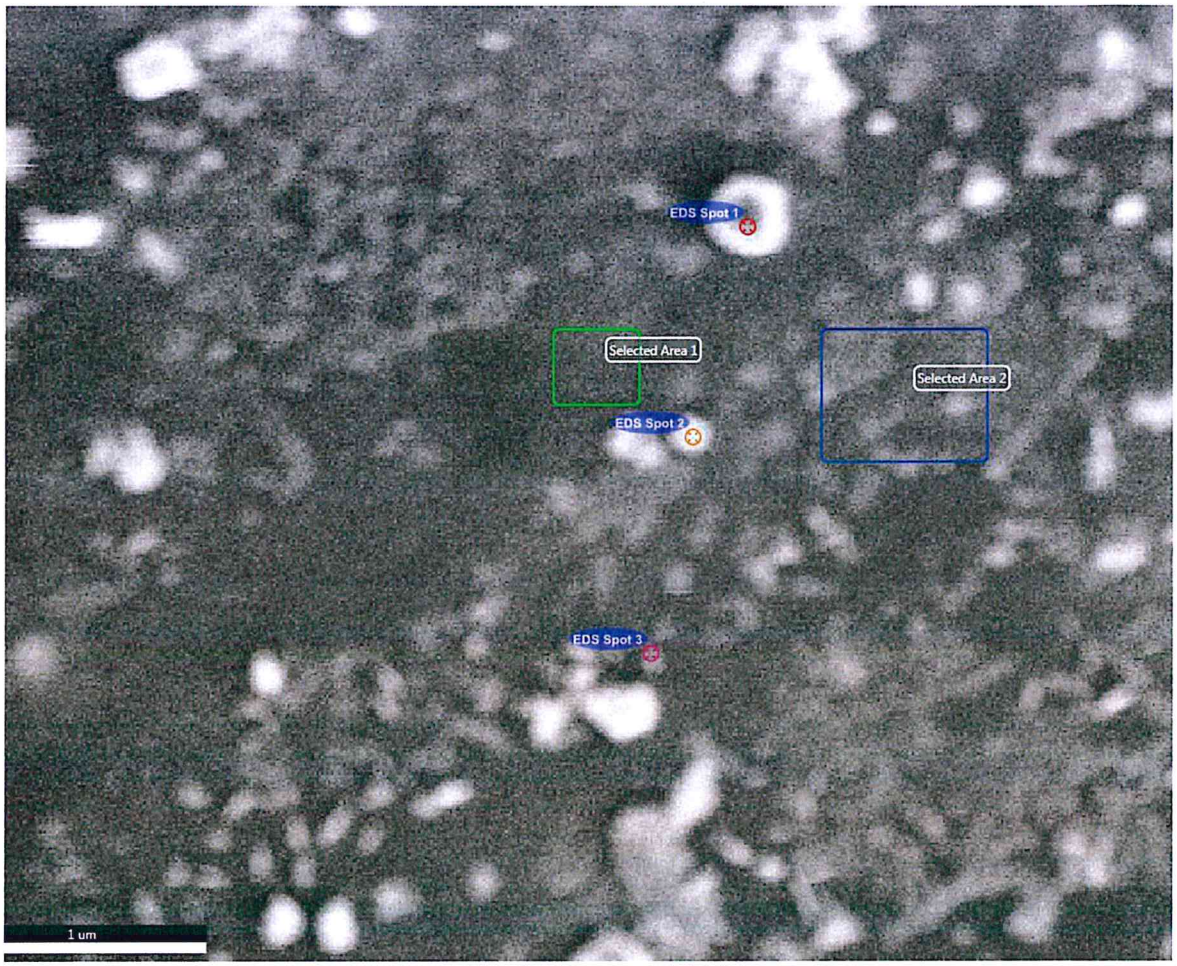

Figure 4.3: SEM image for Ag(O)/As(O) thick film.

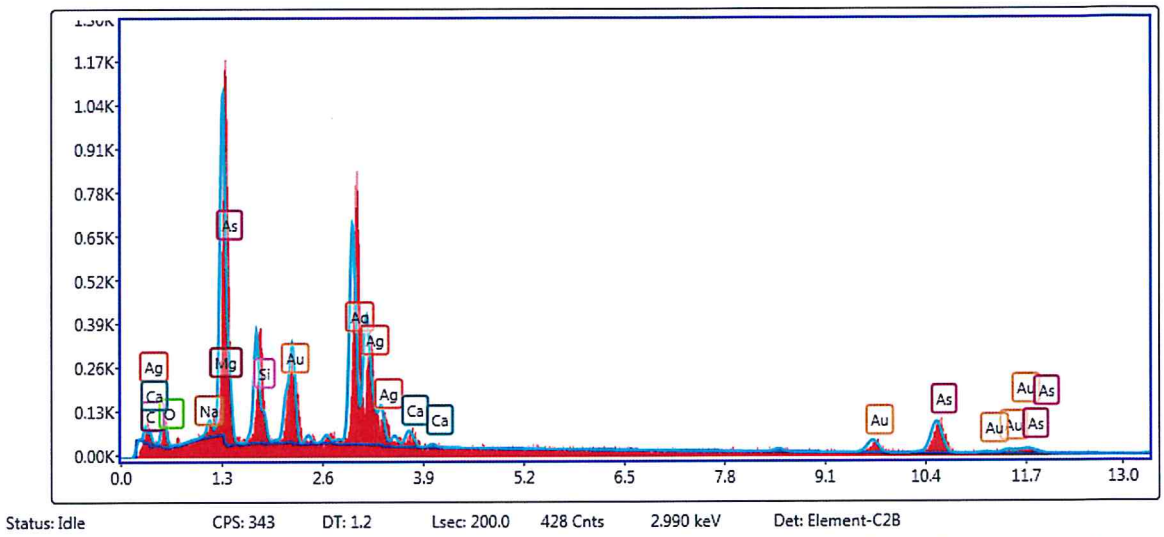

Figure 4.4: The EDS for the Ag(O)/As(O) thick film from points 1, 2 and 3, respectively.

The results of the EDS for spot 1 are shown in the Table 4.4. In accordance with the table the atomic% for the As is 53.64% and for Ag has a value of 0.64%. As a result, the spot 1 is mostly arsenic, the other are glass related. Table 4.5

Table 4.4: The results of the EDS for spot 1 for the Ag(O)/As(O) thick film.

Element	Atomic%
C K	0.39
O K	38.02
Na K	0.22
Mg K	0.02
Si K	1.76
Ag L	0.64
Ca K	0.39
Au L	4.94
As K	53.64

As seen from Table 4.5, the results of the EDS for spot 2 have shown that the spot is a mix of As and Ag. The atomic% for the As and Ag have a value of 13.67% and 21.72%, respectively. The ratio of As compared to the Ag is almost 0.38%. The results of the EDS for spots 3 are tabulated in Table 4.6. Its clear from the table that spot 3 is rich with Ag with an atomic% of 47.4%.

Table 4.5: The results of the EDS for spot 2 for the Ag(O)/As(O) thick film.

Element	Atomic%
C K	0
O K	62.6
Na K	0
Mg K	0.2
Si K	1.81
Ag L	21.72
Ca K	0
Au L	0
As K	13.67

Table 4.6: The results of the EDS for spot 3 for the Ag(O)/As(O) thick film.

Element	Atomic%
C K	0.74
O K	0.98
Na K	0
Mg K	0.15
Si K	41.8
Ag L	47.7
Ca K	0.11
Au L	7
As K	1.53

4.2: Optical properties:

To reveal the effect of the arsenic oxide thin films on the optical properties of the Ag(O) thin film, the transmittance and reflectance spectra are explored by means of ultraviolet-visible light spectroscopy. The transmittance and reflectance spectra are illustrated in Fig.4.5 (a) and (b), respectively. It is clear from the figure that Ag(O) acts like a metal as the transmittance decreases with increasing incident light wavelength in the visible region of light [31]. In addition, the maximum transmittance observed at 364 nm. While the reflectance of Ag(O) thin film decreased in the infrared region of light reaching a minima at 324 nm, it increased in the visible region of light reaching a maximum at λ of 592 nm. It decreased to 850 nm and increased to 1098 nm as the figure show, this is called a Plasmon resonance. It occurred when Ag(O) thin film are interfaced with a dielectric medium [32]. The transmittance of arsenic oxide film behaves like semiconductors. The reflectance of arsenic films also increases with increasing wavelength. Furthermore, for the Ag(O)/As(O) thin film, the transmittance acts as semiconductor like the arsenic oxide film and the reflectance acts as the arsenic but in different way.

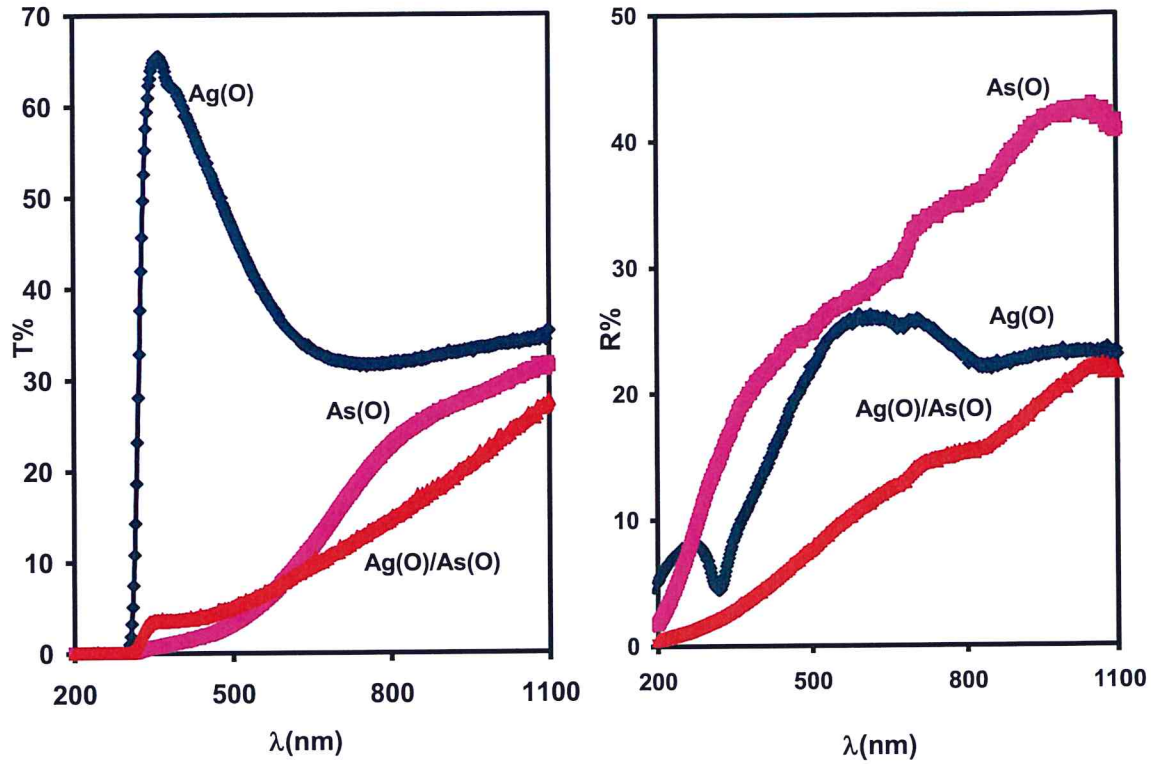

Figure4.5. (a) The transmittance and (b) reflectance for Ag(O), As(O), Ag(O)/As(O) thin films.

The measured transmittance and reflectance spectra which are studied in the range of 190-1100 nm for the Ag(O), arsenic oxide and Ag(O)/As(O) are utilized to determine the absorption coefficient (α) through the equation $\alpha = -\frac{\ln\left(\frac{T}{(1-R_g)(1-R_{sample})}\right)}{d}$. The absorption coefficient spectra are presented in Figure 4.6 (a). As seen from the figure, the absorption coefficient values glass/As(O) film sharply decrease with decreasing the incident photon energy in the range 4.1-3.5 eV. It then gradually decreases until reaching lower energy values. On the other hand, the α-spectra for glass/Ag(O) films exhibit much lower value than that of glass/As(O) films. In the incident photon range of 3.4-1.1 eV, α-spectra displays increasing trends of variation with decreasing incident light energy value. The α-spectra values of Ag(O)/As(O) films follows two trends of variations being dominant in the region of 4.2-3.6 eV and below 2.5 eV, respectively.

The α-spectra values slightly re-increase in the range 3.6-2.5 eV. The absorption coefficient values for Ag(O)/As(O) being lower than those of As(O) in the range 4.1-2.4 eV and higher than that in the lower range of light (below 1.8 eV). The increase in α-spectra values indicates the existence of free carrier absorption on the metal surface. The free carrier absorption is assigned to the transition of carriers from the conduction to the valence band [33].

To get clearer picture about the variations in the spectral absorption ratio (R_λ) of the arsenic oxide, the absorbability are calculated using the rule $R_\lambda = \frac{\alpha_{Ag(O)/As(O)}}{\alpha_{As(O)}}$. The absorbability ($R_\lambda$) spectra is illustrated in figure 4.6 (b). As the figure show, the coating of arsenic oxide onto the Ag(O) films enhanced the light absorbability in the spectral range of 1.9-1.1 eV in infrared region. The highest possible absorbability value is 1.8 at 1.2 eV.

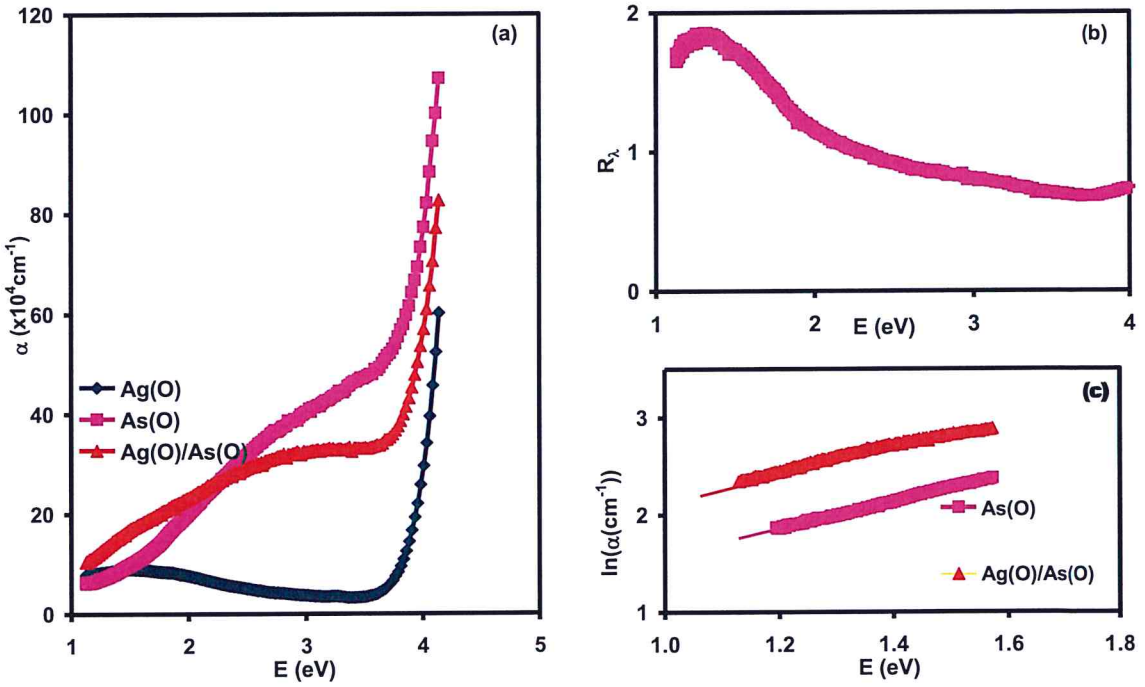

Figure 4.6. (a) The absorption coefficients spectra of As(O) and Ag(O)/As(O) thin films. (b) The absorbability (R_λ) spectra for arsenic thin films. (c) The ln(α) – E variations for the As(O) and Ag(O)/As(O) films.

It is also noticeable from the figure that the absorption coefficient for two samples in the lowest energy range (1.9-1.1 eV) decreases with decreasing incident photon energy indicating the presence of band tails. The band tails are formed by defects, impurities and inhomogeneities [34]. In the low absorption region, where the band tail is supposed to exist, the α values can be presented by $\alpha = \alpha_0 \exp(\frac{E}{E_u})$ [35]. Where, α_0 is constant and E_u is the band tail energy (or urbach energy). The energy band tails usually refers to the presence of defects in the structure. The existence of defects lead to a decrease in the carrier concentration and weakening of the low band tails [36]. The E_u can be estimated by measuring the reciprocal of linear slop of $\ln(\alpha) - E$ variations [37] which are presented in Fig.4.6 (c). Furthermore, the calculated values of the band tail energy are found to be 0.715 eV and 0.793 eV for As(O) and Ag(O)/As(O), respectively. These band tail energy levels may also be attributed to the recombination mechanism as a result of defects [34].

The absorption coefficient spectra reveal an information about the optical changes that arises from the stacking of the films. The optical transitions are estimated from the absorption coefficient spectra through the execution of the Tauc's equation $(\alpha E)^{1/3} = B(E - E_g)$ [34]. The $(\alpha E)^{1/3}$ - E variations are illustrated in Fig.4.7. As seen from the figure 4.6 (a) the E-axis crossings indicate an indirect allowed energy band gap of 2.67 eV for Ag(O)/As(O) films. The E-axis crossings in Fig. 4.7 (a) and (b) reveal two indirect allowed transitions band gaps of glass/As(O) thin films of values of 2.41 eV and 1.43 eV, respectively. The indirect energy gap for arsenic oxide is performed from the spin orbit coupling along the Γ - T line of the first Brillouin zone [37]. The silver oxide substrate effects on the energy gap for arsenic films is compared with the Ag/CdO thin films, the Ag substrate decreased the band gap of CdO. In

addition, the Ag metal improved the structural and electrical properties of CdO thin films [38]. The literature data reported a band gap value of 2.21 eV for glass/arsenic oxide monolayers [39].

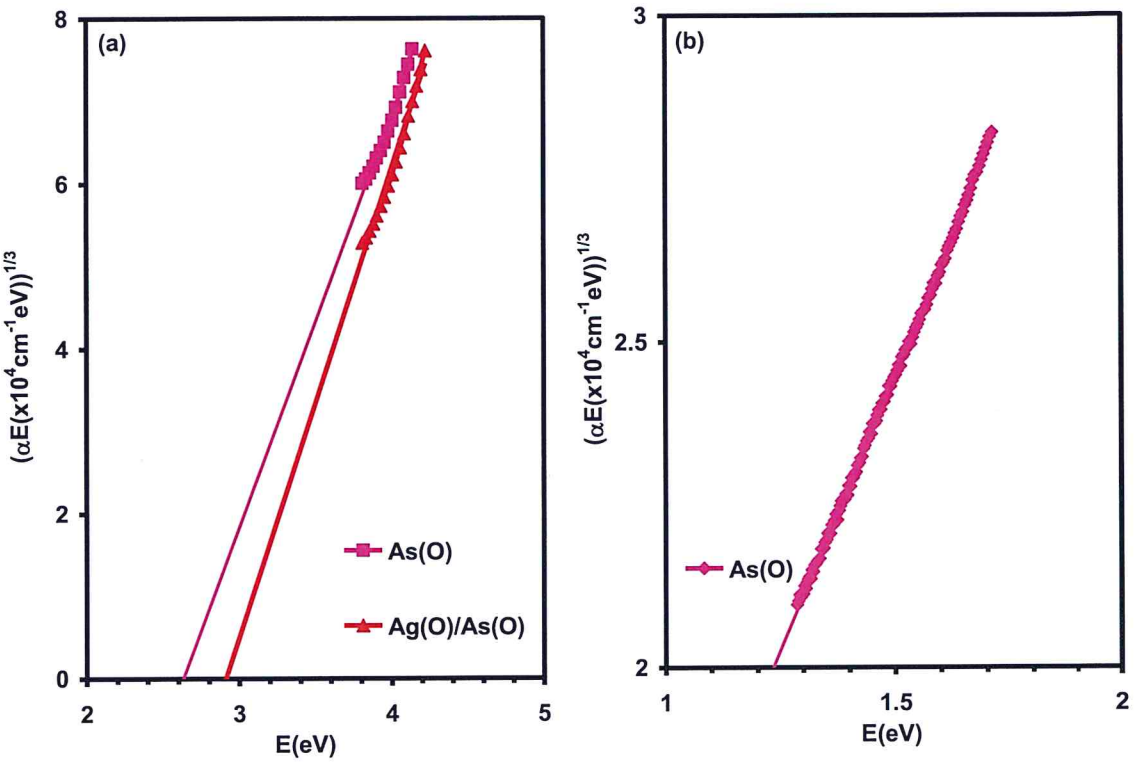

Figure 4.7. The Tauc's equation plotting for (a) As(O) and Ag(O)/As(O) thin films. (b) arsenic oxide thin films.

To observe possible applications of the studied films. The dielectric properties of Ag(O), As(O) and Ag(O)/As(O) are investigated. The effective dielectric constant is calculated through applying Fresnel's equation for the light propagating at normal incidence.

The calculated real dielectric constant spectra (ε_r) for the studied samples is presented in Fig.4.8. As the figure shows, the real part of dielectric constant for Ag(O) exhibits one peak centered at 1.75 eV, this peak should correspond to interband transition in Ag(O) which emerges from the defects and broken bonds on the structure [34]. While the ε_r spectra for arsenic display a peak at

1.18 eV and shoulder located at 1.72 eV, the ε_r spectra of Ag(O)/As(O) decreases with the presence of arsenic oxide are possibly due to less contribution of charge accumulation at the interface of the Ag(O) films [34]. In the spectral region 1.76-1.48 eV, the dielectric constant of Ag(O) decreases and that of Ag(O)/As(O) increases with decreasing incident photon energy. As it is also readable from the figure, the ε_r spectra of Ag(O), As(O), Ag(O)/As(O) there is a Plasmon frequency located at energy values of 4.22 eV, 4.06 eV and 3.98 eV, respectively. The existence of Plasmon resonance is due to the electric field at the interface between the metal and semiconductor [40]. In addition, it arises from resonant absorption [41] and generation of electron hole pairs [42]. As readable from Fig. 4.8, the dielectric constant exhibits a negative values in the incident photon energy range of 4.14-4.28 eV. The existence of the negative ε_r spectra arises from the frequencies of the electron motion that is lower than the plasma frequency [43], and the metallic nature of the material [44].

On the other hand, the imaginary part ε_{im} of dielectric constant spectra for Ag(O), As(O), and Ag(O)/As(O) which appears in Fig.4.9 display different variation when compared to the real part spectra. Its clear from the Fig.4.9 (a) that in the photon energy range of 2.65-1.12 eV, ε_{im} increases with decreasing incident photon energy for Ag. In the same context, the ε_{im} for arsenic oxide exhibits a peak located at 2.7 eV. In the energy region of 1.52-2.56 eV, ε_{im} increases with increasing photon energy. It then decreases with increasing energy in the region of 2.7-3.6 eV. In addition, the coating of arsenic oxide on the Ag(O) decreases the ε_{im} reaching 5.91 at an incident photon energy value of 4.19 eV.

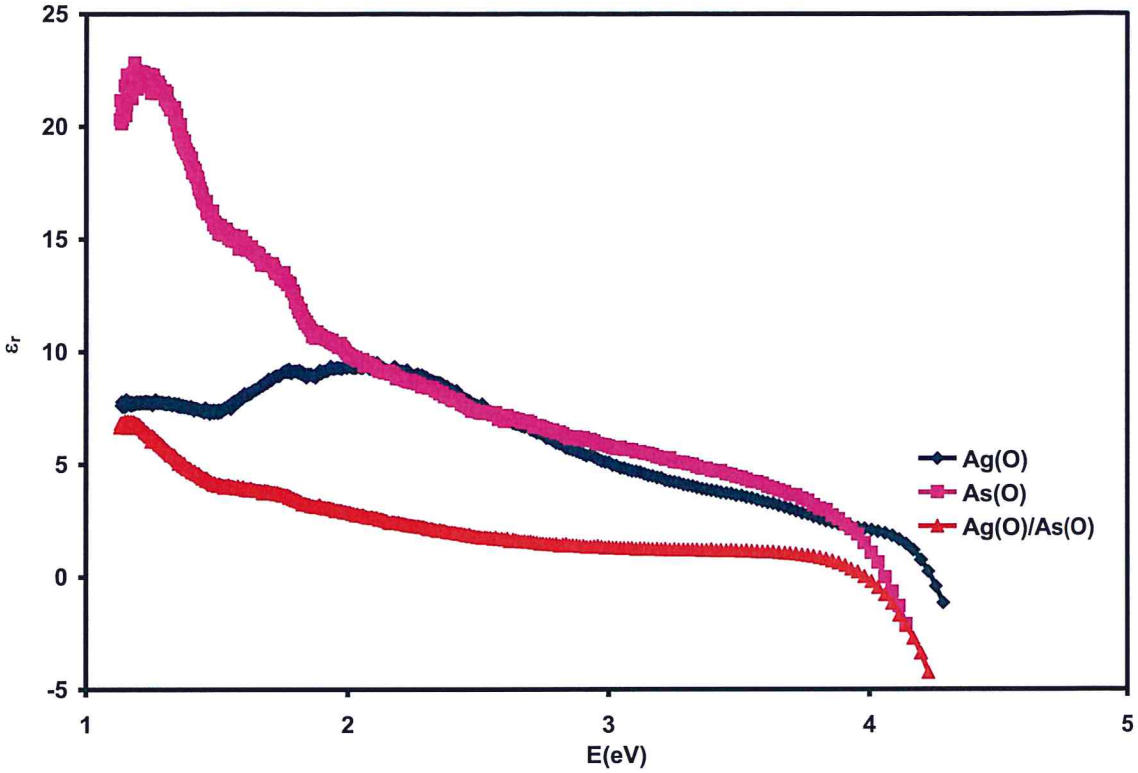

Figure 4.8: The real part of dielectric spectra for Ag(O), As(O), Ag(O)/As(O) thin films.

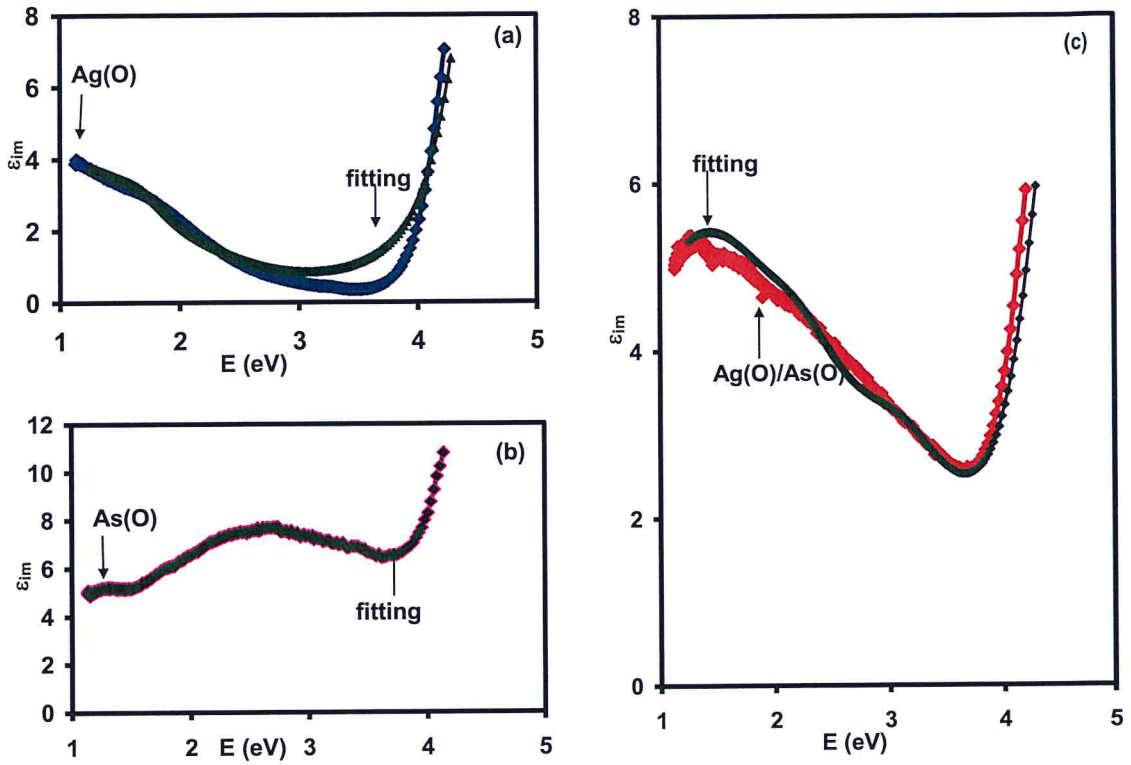

Figure 4.9: imaginary part of dielectric spectra constant for (a) Ag(O), (b) As(O) and (c) Ag(O)/As(O) thin films, respectively. The black colored plots in (a), (b) and (c) illustrate the fitting of Drude-Lorentz equation.

The importance of imaginary part of dielectric constant spectra emerges from its direct relation to the optical conductivity σ(ω) as $\varepsilon_{im} = \sum_{i=1}^{k} \frac{\omega_{pei}^2 \omega}{((\omega_{ei}^2 - \omega^2) + (\omega^2 \tau_i^{-2}))}$. The larger ε_{im}, the higher optical conductivity. By applying Drude-Lorentz relation, the experimental data were reproduced to determine the optical conductivity parameters. Assuming the effective mass of electrons for Ag(O) of 1.0 m_o [45], and 1.25 m_o for arsenic oxide, the reduced effective mass m* is determined as 0.556 m_o. The black colored plots of Fig.4.8 display the outcomes of fitting of the Drude-Lorentz equation. Table 4.7, 4.8, 4.9 show the fitting parameters with the experimental and theoretical imaginary part of dielectric constants spectra for the Ag(O), As(O), Ag(O)/As(O) thin films, respectively. As readable from the table, five linear oscillators are needed to

reproduce the ε_{im}-E variation of the Ag(O), As(O), Ag(O)/As(O), respectively. The electron scattering time decreased when arsenic is coated onto Ag(O) from 0.8 fs to 0.5 fs. The drift mobility which exhibit value of 1.40 cm^2/Vs for Ag increased to 1.58 cm^2/Vs upon coating of arsenic oxide. This improvement in the drift mobility of Ag(O) arose from the decrease in defects that is related to the variation of carrier concentration [34]. In the scope of these observations, the enhancement of mobility μ for Ag(O)/As(O) might be assigned to the reduction in dislocation density as the XRD analysis showed.

Moreover, the free electron density for Ag(O), As(O) and Ag(O)/As(O) are found to be 1.6 x 10^{20}, 2.8 x 10^{20} and 1.5 x 10^{20} cm^{-3}, respectively. In addition, the electron plasma frequency ω_p increases for Ag(O)/As(O) thin film from 7.5 GHz to value of 9.8 GHz and the resonance frequency ω_e is not affect by arsenic oxide.

As seen from Table 4.7 and 4.9, it is clear that arsenic stacking layer improves the optical conduction parameters. The high mobility makes the Ag(O)/As(O) a good candidate as a thin film transistor [34]. The free electron density increases the Plasmon frequency when arsenic oxide is coated. This increase related to the presence of additional free electrons on the metal surface [34].

Table 4.7 : Optical conductivity parameters for Ag(O) thin films being computed with the Drude-Lorentz model.

K	1	2	3	4	5
τ(fs)	0.8	0.8	0.5	0.5	1.2
n ($x10^{19}$ cm^{-3})	16	13	10	10	120
ω_e ($x10^{15}$ Hz)	1.9	2.6	3.5	6.2	6.75
ω_p (GHz)	7.5	6.8	5.9	5.9	20.6
μ (cm^2/Vs)	1.40	1.40	0.87	0.87	2.10

Table 4.8 : Optical conductivity parameters for As(O) thin films being computed with the Drude-Lorentz model.

K	1	2	3	4	5
τ(fs)	0.4	0.45	0.38	0.39	0.7
n ($x10^{19}$ cm^{-3})	28	28	28	190	550
ω_e ($x10^{15}$ Hz)	1.6	2.8	3.5	4.4	7
ω_p (GHz)	8.9	8.9	8.9	23.2	39.4
μ (cm^2/Vs)	0.77	0.63	0.53	0.54	0.98

Table 4.9 : Optical conductivity parameters for Ag(O)/As(O) thin films being computed with the Drude-Lorentz model.

K	1	2	3	4	5
τ(fs)	0.5	0.5	0.5	0.5	1
n ($x10^{19}$ cm^{-3})	15	15	20	21	60
ω_e ($x10^{15}$ Hz)	1.9	2.6	3.5	4.8	6.7
ω_p (GHz)	9.8	9.8	11.3	11.6	19.5
μ (cm^2/Vs)	1.58	1.58	1.58	1.58	3.16

4.3: Capacitance-Voltage Characteristics:

The Fig. 4.10(a) represent the capacitance-voltage characteristic curve for the Ag(O)/As(O)/C device. The curve is recorded at signal frequency of 1.0 MHz. The C-V curve illustrates a metal oxide semiconductor field effect transistors (MOSFET) characteristic curve. Particularly, the device displays PMOS transistor characteristics when reverse biased and NMOS transistor when forward biased [46]. The hot probe technique tests on the grown films showed that the arsenic oxide, Ag(O), Ag(O)/As(O) films exhibit n-type conductivity. Since, the work function of carbon being 5.1 eV [47] is greater than that of arsenic (2.01 eV), schottky diode is formed at the As(O)/C side. As the work function of Ag(O) being 4.74 eV [48] is less than that of As(O), Ag(O)/As(O) form ohmic contact. The built in potential at the As(O)/C arm is ($V_{bi} = q\varphi_C - q\varphi_{As}$) =3.1 eV. The electron affinity (qχ) of arsenic is 0.81 eV [49] and that of Ag is 1.30 eV [50]. Due to the difference in the electron affinities the vacuum level of C is lowered. Analysis of the C-V curve with respect to the depletion capacitance equation $C^{-2} = 2(V - V_{bi} - ({}^{KT}/_{q}))/(qA^2\varepsilon_s N_a)$ [46] in the depletion range in the NMOS or PMOS detects the slopping line which is illustrated in Fig.4.9 (b) and (c), respectively. In accordance with the slope of the curve which are presented for MOS device of an area of 3.14×10^{-2} cm^2 the built in potential value is 3.54 eV in the depletion region. The free carrier concentration and depletion width are tabulated in Table 4.10. The difference between the values that is determined experimentally from the C-V curves to those that are theoretically calculated is ascribed to many reasons like the frequency dependence of the built in voltage, surface traps and surface charges [46].

Table 4.10

1 MHz	ε_{Ag}	ε_{As}	ε	V_{bi} (V)	N×10^{17}	W(Å)
forward	3	5	1.8	3.5	9.0	1
reverse	3	5	1.8	3.6	9.1	1

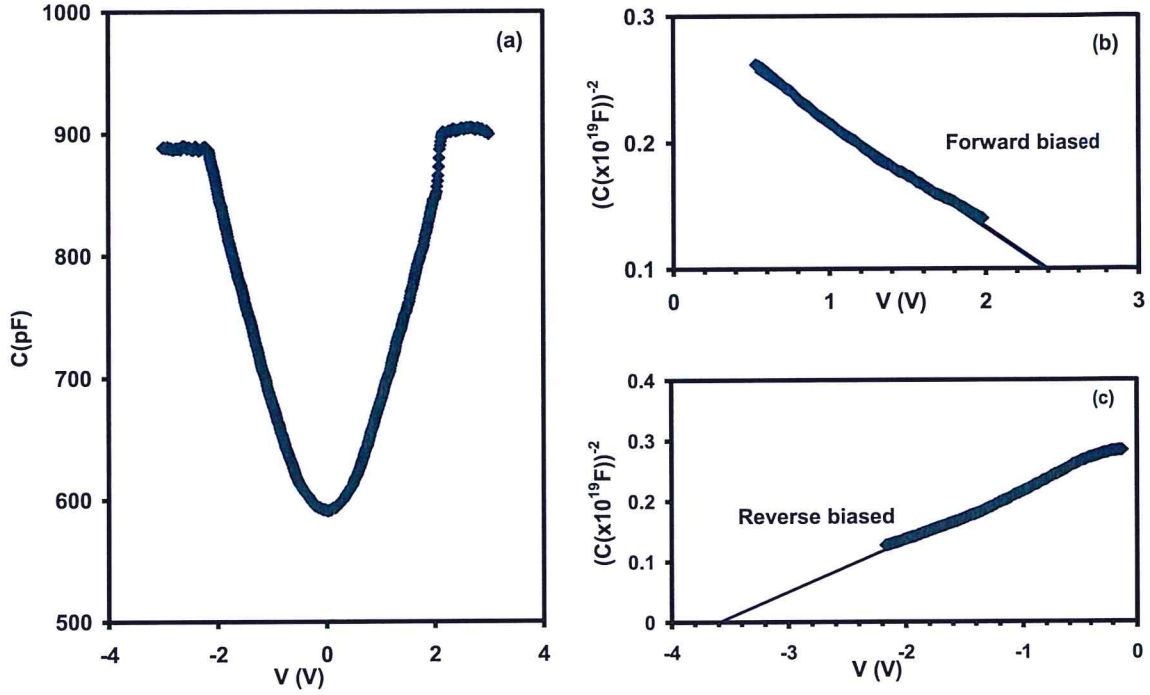

Figure 4.10: (a) The capacitance voltage characteristics for Ag(O)/As(O)/C device at 1 MHz frequency, (b), and (c)The C^{-2} – E variations for the device in forward, reverse biasing, respectively.

4.4: Impedance spectroscopy analysis:

In order to find the practical applications for the Ag(O)/As(O)/C device, the samples where contacted with carbon point contact of an area of 3.14×10^{-3} cm^2. The geometrical design of Ag(O)/As(O)/C device is illustrated in the inset of figure 4.10(a). The device was imposed between the electrodes of the impedance analyzer operative in the frequency range of 0.01-1.80 GHz. The measured capacitance (C) and conductance (G) spectra are illustrated in figure 4.10. Figure 4.11 (a) shows an interesting feature of the capacitance spectra. As Fig 4.11 (a) shows, the capacitance illustrates positive values and increases with increasing frequency in the frequency range of 0.269-0.307 GHz, where it reaches a maxima. It then sharply decreases reaching a negative value of minima centered at 0.316 GHz. The capacitance show a negative value in the frequency domain of 0.316-0.405 GHz. In addition, the capacitance exhibits resonance-antiresonance phenomena that are associated with the negative capacitance (NC) effect. The width of the switching peaks is 11.0 MHz. Furthermore, the negative capacitance effect indicates the ability of using Ag(O)/As(O) device for noise reduction in radio wave/microwave and as signal amplifiers [51]. NC effect emerges from minority carrier injections caused by accumulation of minority carriers at the grain boundaries [51]. On the other hand, Fig.4.10 (b) presents the conductance spectra (G) of the Ag(O)/As(O)/C device. The conductance spectra displayed peaks located at 0.29 GHz, 1.163 GHz and 1.477 GHz, respectively. Moreover, the peaks that appeared in the G spectra can be ascribed to the excitation and hoping processes [52]. The previous studies on oscillatory conductance have shown that it is influenced by differential negative effective density of states at specific values of carrier concentrations [52].

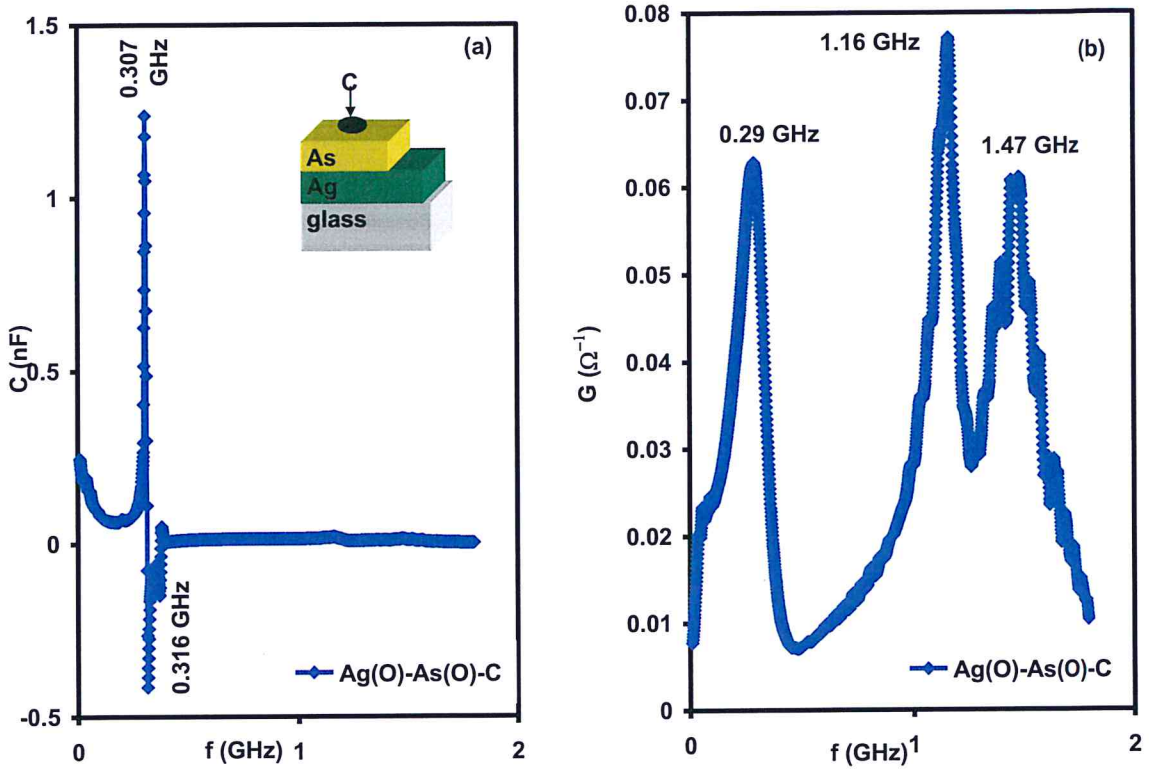

Figure 4.11: (a) The capacitance and (b) conductance spectra for the thick Ag(O)/As(O)/C device. The inset of (a) display a geometrical design of the device.

The calculated impedance spectra (Z) for Ag(O)/As(O)/C devices are illustrated in Fig.4.12 (a). As the figure show, the impedance spectra decrease with increasing frequency displaying one local and one absolute minima at 0.39 GHz and at 1.23 GHz, respectively. The impedance spectra are used to determine the magnitude of reflection coefficiant spectra ρ. The magnitude of reflection coefficient spectra is displayed in Fig.4.12 (b). ρ spectra illustrated notch frequencies (f_n) at 0.056 GHz, 0.373 GHz and 1.215 GHz, respectively. It indicates that Ag(O)/As(O)/C device behaves like a band pass filter. In addition, the return loss spectra (L_r) that is important in telecommunication technology are presented in Fig.4.12 (c). The acceptable value of return loss should exceed 20 dB [53]. The value of L_r at the notch frequency (0.373 GHz) is 27 dB implying good matches between the Ag(O)/As(O)/C device and the signal source.

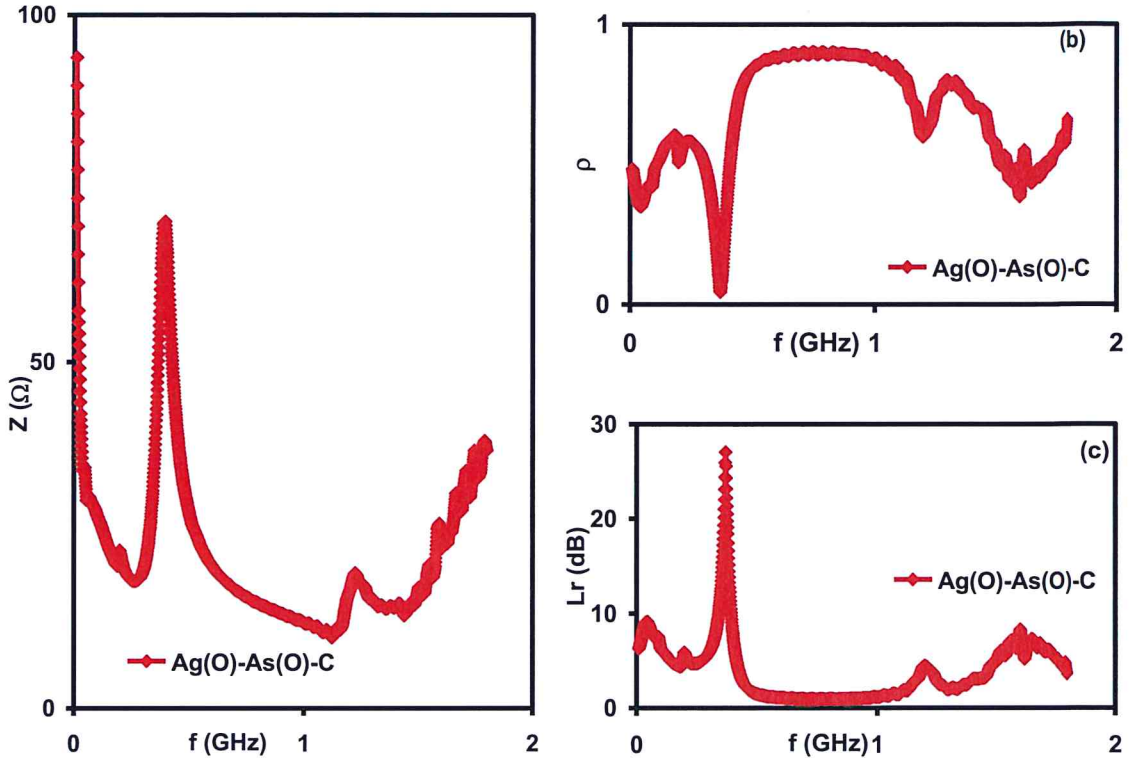

Figure 4.11: (a) The impedance, (b) the magnitude of the reflection coefficient and (c) the return loss spectra for Ag(O)/As(O) device.

Chapter Five

Conclusion

In this thesis, we attempt to explore the structural, optical and electrical properties of arsenic oxide films which are coated onto glass and Ag(O) substrates. The As oxide films which were grown by the thermal evaporations technique are of amorphous nature. The influence the crystallinty of the Ag(O) substrates are also studied. Arsenic oxide films are also observed to exhibit two energy band gaps being dominant in the visible and infrared ranges of light. Interfacing of As(O) with Ag(O) resulted in enhanced light absorbability in the IR range. It is also observed that the simple structure of Ag(O)/As(O) can be recommended as promising plasmonic interface exhibiting Plasmon resonance near 20 GHz. This feature is attractive for 5G mobile technologies. In addition, coating of As(O) onto Ag(O) enhanced the drift mobility of e's making it more appropriate for thin film transistor technology. This possibility is tested via capacitance (C)-voltage (V) characteristics measurements. The C-V curves displayed MOSFET device features. As mosfets, they were found suitable for use as band pass/reject filters with notch frequency values being dominant in the microwave range of frequency.

References:

[1] Elias, J. (2019). Experimental investigations on the effect of addition of Ag into ternary lead free solder alloy Sn-1Cu-1Ni. *Letters on Materials, 9(2),* 239-242.

[2] Tsai, T. Y., Chen, P. F., Chang, S. W., & Wu, Y. R. (2021). Studies of 2D bulk and nanoribbon band structures in MoxW1–xS2 Alloy System Using Full sp3d5 Tight- Binding Model. *Physica status solidi (b), 258(2),* 2000375.

[3] Sadullah, M., Kaur, J., Basu, R., & Sharma, A. K. (2020). Analysis of thin-film direct band-gap SiGeSn alloy based heterostructure solar cell featuring SiGe absorber layer. *Optik, 202,* 163715.

[4] Wang, H., Guo, T., Xue, Y., Lv, S., Yao, D., Zhou, Z., ... & Song, Z. (2019). The phase change memory features high-temperature characteristic based on Ge-Sb-Se-Te alloys. *Materials Letters, 254,* 182-185.

[5] Yu, M., Li, H., Gao, F., Hu, Y., Wang, L., Hu, P., & Feng, W. (2020). Synthesis of Multilayer InSe0. 82Te0. 18 alloy for high performance near-infrared photodetector. *Journal of Alloys and Compounds, 815,* 152375.

[6] Askarnia, R., Ghasemi, B., Fardi, S. R., & Adabifiroozjaei, E. (2020). Improvement of tribological, mechanical and chemical properties of Mg alloy (AZ91D) by electrophoretic deposition of alumina/GO coating. *Surface and Coatings Technology, 403,* 126410.

[7] Aulakh, S. S., & Kaushal, G. (2019). Laser texturing as an alternative to grit blasting for improved coating adhesion on AZ91D magnesium alloy. *Transactions of the IMF, 97(2),* 100-108.

[8] Parida, S. K., Mohanta, M., Sahoo, M. A., Meher, R., & Medicherla, V. R. R. Research of Mechanical Properties of Random Disordered CuNi Alloys.

[9] Cai, H., Guo, F., Su, J., & Liu, L. (2019). Existing forms of Gd in AZ91 magnesium alloy and its effects on mechanical properties. *Materials Research Express, 6(6),* 066541.

[10] Badi, N., Al-Douri, Y., & Khasim, S. (2019). Effect of nitrogen doping on structural and optical properties of MgxZn1-xO ternary alloys. *Optical Materials, 89*, 554-558.

[11] Gomes, L. F., da Silva, P. S., Garcia, A., & Spinelli, J. E. (2020). Effects of Silver Content and Cooling Rate on Electrical Conductivity and Tensile Properties of Al-Si (-Ag) Alloys. *Journal of Materials Engineering and Performance, 29(10),* 6849-6860.

[12] Shaban, M., Kholidy, I., Ahmed, G. M., Negem, M., & Abd El-Salam, H. M. (2019). Cyclic voltammetry growth and characterization of Sn–Ag alloys of different nanomorphologies and compositions for efficient hydrogen evolution in alkaline solutions. *RSC advances, 9(39),* 22389-22400.

[13] Sharma, A., Chung, C. H., & Ahn, B. (2019). Pulse co-deposition of tin-silver alloy from citric acid plating bath for microelectronic applications. *Materials Research Express, 6(11),* 1165g8.

[14] Zareidoost, A., & Yousefpour, M. (2020). A study on the mechanical properties and corrosion behavior of the new as-cast TZNT alloys for biomedical applications. *Materials Science and Engineering: C, 110*, 110725.

[15] Rasul, M. N., Javed, A., Khan, M. A., & Hussain, A. (2019). Study of the structural, mechanical, electronic and magnetic properties of quaternary YFeCrX (X= Al, Ga, In, Si, Ge, Sn, P, As, Sb) Heusler alloys. *Journal of Magnetism and Magnetic Materials, 476*, 398-411.

[16] Fortin- Deschênes, M., Waller, O., An, Q., Lagos, M. J., Botton, G. A., Guo, H., & Moutanabbir, O. (2020). 2D Antimony–Arsenic Alloys. *Small, 16(3)*, 1906540.

[17] Karki, B., Rajapakse, M., Sumanasekera, G. U., & Jasinski, J. B. (2020). Structural and thermoelectric properties of black arsenic–phosphorus. *ACS Applied Energy Materials, 3(9),* 8543-8551.

[18] Bouša, D., Otyepková, E., Lazar, P., Otyepka, M., & Sofer, Z. (2020). Surface Energy of Black Phosphorus Alloys with Arsenic. *ChemNanoMat, 6(5),* 821-826.

[19] Kittel, C., McEuen, P., &McEuen, P. (1996). Introduction to solid state physics (Vol. 8, pp. 105-130). New York: Wiley.

[20] Qasrawi, A. F., & Omareya, O. A. (2019). In situ observations of the permanent structural modifications, phase transformations and band gap narrowing upon heating of Cu2Se/Yb/Cu2Se films. Journal of Alloys and Compounds, 785, 1160-1165.

[21] Kulawiak, M., &Chybicki, A. (2018). Application of Web-GIS and geovisual analytics to monitoring of seabed evolution in South Baltic Sea coastal areas. Marine Geodesy, 41(4), 405-426.

[22] Fox, M. (2002). Optical properties of solids.

[23] AlGarni, S. E., & Qasrawi, A. F. (2020). Nonlinear optical performance of CdO/InSe Interfaces. *Physica Scripta, 95(6),* 065801.

[24] Pankove, J. I. (1975). Optical processes in semiconductors. Courier Corporation.

[25] Wager, J. F. (2017). Real-and reciprocal-space attributes of band tail states. AIP Advances, 7(12), 125321.

[26] Attwood, David (1999). Soft X-rays and extreme ultraviolet radiation: principles and applications. p. 60. ISBN 978-0-521-02997-1.

[27] Parida, S., Rout, S. K., Barhai, P. K., & Bera, J. (2012). Influence of ball milling parameters on the crystallite size of Ba (Ti1-xZrx) O3. *Ferroelectrics, 429(1),* 22-30.

[28] Djafar, R., Boumchedda, K., Chaouchi, A., Fasquelle, D., Sedda, K., Brahimi, S., ... & Bououdina, M. (2020). Cu2O addition and sintering temperature dependence of structural, microstructural and dielectric properties of CaCu3Ti4O12 ceramics. *Materials Chemistry and Physics, 256,* 123706.

[29] Ruzgar, S., Caglar, Y., & Caglar, M. (2020). The influence of low indium composition ratio on sol–gel solution-deposited amorphous zinc oxide thin film transistors. *Journal of Materials Science: Materials in Electronics*, *31*, 11720-11728.

[30] Inoue, M., Urai, N., & Yagi, H. (1979). Amorphous nature of vacuum-deposited Bi□ Sb alloy films. *Surface Science*, *86*, 369-377.

[31] Ching, S. Y. (2016). Plasmonic properties of silver-based alloy thin films.

[32] Al Garni, S. E., Omar, A., & Qasrawi, A. F. (2017). Plasmon interactions at the (Ag, Al)/InSe thin-Film interfaces designed for dual Terahertz/Gigahertz applications. *Plasmonics, 12(2),* 515-521.

[33] Qasrawi, A. F., & Aloushi, H. D. (2019). In situ monitoring of the permanent crystallization, phase transformations and the associated optical and electrical enhancements upon heating of Se thin films. *Physica B: Condensed Matter, 569,* 62-67.

[34] Qasrawi, A. F. (2019). Effect of Y, Au and YAu nanosandwiching on the structural, optical and dielectric properties of ZnSe thin films.

[35] Ng, B. J., Putri, L. K., Kong, X. Y., Pasbakhsh, P., & Chai, S. P. (2020). Overall pure water splitting using one-dimensional P-doped twinned Zn0. 5Cd0. 5S1-x nanorods via synergetic combination of long-range ordered homojunctions and interstitial S vacancies with prolonged carrier lifetime. *Applied Catalysis B: Environmental, 262,* 118309.

[36] Liu, H. F., Chua, S. J., Hu, G. X., Gong, H., & Xiang, N. (2007). Annealing effects on electrical and optical properties of ZnO thin-film samples deposited by radio frequency-magnetron sputtering on GaAs (001) substrates. *Journal of Applied Physics, 102(6),* 063507.

[37] Gonze, X., Michenaud, J. P., & Vigneron, J. P. (1990). First-principles study of As, Sb, and Bi electronic properties. *Physical Review B, 41(17),* 11827.

[38] Mostafa, A. M., & Mwafy, E. A. (2020). Laser-assisted for preparation Ag/CdO nanocomposite thin film: Structural and optical study. *Optical Materials, 107,* 110124.

[39] Chun-Ying, P., Xiao-Tao, Y., Hua-Long, J., Fei-Wu, Z., Zhi-Wen, L., Jun-Bao, H., & Da-Wei, Z. (2015). Two-dimensional arsenic monolayer sheet predicted from first-principles. *Chinese Physics B, 24(3),* 036301.

[40] Mahanti, M., & Basak, D. (2012). Highly enhanced UV emission due to surface plasmon resonance in Ag–ZnO nanorods. *Chemical Physics Letters, 542,* 110-116.

[41] Foroutan, V. (2020). Numerical study of the homogeneous and inhomogeneous magnetic field effects on the plasma-based radar cross-section reduction. *IET Radar, Sonar & Navigation, 14*(3), 468-476.

[42] Yang, T., Ge, J. C., Li, X. A., Stantchev, R. I., Zhu, Y. Y., Zhou, Y., & Huang, W. (2018). Non-destructive plasma frequency measurement for a semiconductor thin film using broadband surface plasmon polaritons. *Optics Communications, 410,* 926-929.

[43] Chern, R. L., Chang, C. C., & Chang, C. C. (2006). Interfacial operator approach to computing band structures for photonic crystals of polar materials. *Physical Review B, 73*(23), 235123.

[44] Sunku, S. S. (2021). *Twisted bilayer graphene probed with nano-optics.* Columbia University.

[45] Kado, T. (2002). Resonant tunneling through metal (Ag–Ti)/insulator (MgO) triple barrier structures. *Applied physics letters, 80*(18), 3382-3384.

[46] Khusayfan, N. M., & Khanfar, H. K. (2020). Design and Characterization of MoO 3/Mg/MoO 3 Interfaces. *IEEE Transactions on Electron Devices, 67*(10), 4354-4359.

[47] 314003Al Garni, S. E., & Qasrawi, A. F. (2015). Design and characterization of (Al, C)/p- Ge/p- BN/C isotype resonant electronic devices. *physica status solidi (a), 212*(8), 1845-1850.

[48] Khusayfan, N. M., & Khanfar, H. K. (2018). Characterization of CdS/Sb2Te3 micro/nano-interfaces. *Optik*, *158*, 1154-1159.

[49] Sapkota, N. R., & Nakarmi, J. J. (2014). First-Principles Study of Arsenic Atom, Its Irons and Molecule. *Himalayan Physics*, *5*, 17-21.

[50] Guseinov, A. G., Salmanov, V. M., Mamedov, R. M., Dzhabrailova, R., & Magomedov, A. Z. (2018). A New Method of Obtaining an n–p-Structure on the Basis of the Defective Semiconductor AgIn 5 S 8. *Russian Physics Journal*, *60*(10), 1747-1751.

[51] Qasrawi, A. F., & Zyoud, H. M. (2020). Ytterbium induced structural phase transitions and their effects on the optical and electrical properties of ZnPc thin films. *Optical and Quantum Electronics*, *52*(11), 1-12.

[52] Qasrawi, A. F., Abdalghafour, M. A., & Mergen, A. (2021). Tungsten doped Bi1. 5Zn0. 92Nb1. 5O6. 92 ceramics designed as radio/microwave band pass/reject filters. *Microwave and Optical Technology Letters*, *63*(4), 1101-1105.

[53] Qasrawi, A. F. (2020). Characterization of Au/As2Se3 Multifunctional Tunneling Devices. *physica status solidi (a)*, *217*(5), 1900899.

الملخص

تحضير و تشخيص الافلام الرقيقة $AgO-As_2O_3$

في هذه الرسالة ، يتم تصنيع طبقات مكدسة من الفضة المؤكسدة وأكسيد الزرنيخ بواسطة تقنية التبخير الحراري تحت ضغط تفريغ قدره 10-5 ملي بار. نمت فئتان من الأفلام. واحد رقيق (100 نانومتر لكل منهما) والآخر سميك (1.0 ميكرومتر). تتميز الأفلام بتقنيات حيود الأشعة السينية ، ومقياس الطيف الضوئي البصري ، وتقنيات التحليل الطيفي للمقاومة ، على التوالي. وقد لوحظ أن الأفلام القائمة على Ag هي ذات هيكل مكعّب يشتمل على AgO أحادي الميل كمرحلة ثانوية. وزن AgO في الأفلام أقل من 30٪. بينما عرضت أفلام AsO طبيعة غير متبلورة للهيكل. يتم حجز الطبيعة التكعيبية للهيكل في أفلام Ag (O) / As (O) بصريًا ، تعرض أفلام أكسيد الزرنيخ خصائص أشباه الموصلات مع فجوة نطاق طاقة تبلغ 2.41 إلكترون فولت. طلاء اكسيد الزرنيخ على أغشية Ag المؤكسدة عزز امتصاص الضوء لأكسيد الزرنيخ ، يغير اللون الأزرق فجوة نطاق الطاقة ويغير عرض ذيول شريط الطاقة. بالإضافة إلى ذلك ، يتأثر تشتت العزل الكهربائي في أفلام أكسيد As بشدة وينخفض في نطاق الأشعة تحت الحمراء للضوء. سمحت نمذجة الجزء التخيلي من ثابت العزل باستخدام نظرية درود-لورنتز بتحديد معاملات التوصيل البصري. معلمات الموصلية الضوئية التي تقدمها حركة الانجراف وتردد Plasmon مناسبة لتكنولوجيا الاتصالات. يصل تردد Plasmon إلى 20 جيجا هرتز وهو الهدف في تقنيات G5. كهربائيًا ، كشفت خصائص السعة والجهد التي تم تسجيلها بعد ملامسة الأغشية بنقطة تلامس الكربون ، عن خصائص ترانزستور تأثير مجال أكسيد المعدن. الجهد المدمج للجهاز مرتفع بما يكفي لتقنية الأغشية الرقيقة. من ناحية أخرى ، أظهرت دراسات التحليل الطيفي للمقاومة في مجال التردد من 1.0-0.01 جيجاهرتز أن الجهاز يمكن أن يظهر تأثير السعة السلبية المرتبط بظواهر الرنين والرنين المضاد في نطاقات الموجات الراديوية والميكروويف من الأطياف. ميزات الجهاز تجعله مناسبًا لتقنيات الاتصال.